Methods for Homogenization of Spatio-Temporal B_0 Magnetic Field Variations in Cardiac MRI at Ultra-High Field Strength

Methoden zur Homogenisierung räumlicher und zeitlicher Variationen des B_0-Feldes in der kardialen Ultrahochfeld-MRT

Doctoral thesis for a doctoral degree

At the Graduate School of Life Sciences,

Julius-Maximilians-Universität Würzburg,

Section Biomedicine

Submitted by

Michael Hock

Born in

Aschaffenburg

Würzburg, 2023

Submitted on: ……..……

Office stamp

Members of the Thesis Committee

Chairperson: Prof. Dr. Markus Sauer

Primary Supervisor: Prof. Dr. Laura Maria Schreiber, MBA

Supervisor (Second): Prof. Dr. Herbert Köstler

Supervisor (Third): Prof. Dr. Dr. Wolfgang Rudolf Bauer

Date of Public Defence: ……..……

Date of Receipt of Certificates: …….

Summary

Cardiovascular disease is one of the leading causes of death worldwide and, so far, echocardiography, nuclear cardiology, and catheterization are the gold standard techniques used for its detection. Cardiac magnetic resonance (CMR) can replace the invasive imaging modalities and provide a "one-stop shop" characterization of the cardiovascular system by measuring myocardial tissue structure, function and perfusion of the heart, as well as anatomy of and flow in the coronary arteries. In contrast to standard clinical magnetic resonance imaging (MRI) scanners, which are often operated at a field strength of 1.5 or 3 Tesla (T), a higher resolution and subsequent cardiac parameter quantification could potentially be achieved at ultra-high field, i.e., 7 T and above.

Unique insights into the pathophysiology of the heart are expected from ultra-high field MRI, which offers enhanced image quality in combination with novel contrast mechanisms, but suffers from spatio-temporal B_0 magnetic field variations. Due to the resulting spatial misregistration and intra-voxel dephasing, these B_0-field inhomogeneities generate a variety of undesired image artifacts, e.g., artificial image deformation. The resulting macroscopic field gradients lead to signal loss, because the effective transverse relaxation time T_2^* is shortened. This affects the accuracy of T_2^* measurements, which are essential for myocardial tissue characterization. When steady state free precession-based pulse sequences are employed for image acquisition, certain off-resonance frequencies cause signal voids. These banding artifacts complicate the proper marking of the myocardium and, subsequently, systematic errors in cardiac function measurements are inevitable. Clinical MR scanners are equipped with basic shim systems to correct for occurring B_0-field inhomogeneities and resulting image artifacts, however, these are not sufficient for the advanced measurement techniques employed for ultra-high field MRI of the heart.

Therefore, this work focused on the development of advanced B_0 shimming strategies for CMR imaging applications to correct the spatio-temporal B_0 field variations present in the human heart at 7 T. A novel cardiac phase-specific shimming (CPSS) technique was set up, which featured a triggered B_0 map acquisition, anatomy-matched selection of the shim-region-of-interest (SROI), and calibration-based B_0 field modeling. The influence

of technical limitations on the overall spherical harmonics (SH) shim was analyzed. Moreover, benefits as well as pitfalls of dynamic shimming were debated in this study. An advanced B_0 shimming strategy was set up and applied in vivo, which was the first implementation of a heart-specific shimming approach in human UHF MRI at the time.

The spatial B_0-field patterns which were measured in the heart throughout this study contained localized spots of strong inhomogeneities. They fluctuated over the cardiac cycle in both size and strength, and were ideally addressed using anatomy-matched SROIs. Creating a correcting magnetic field with one shim coil, however, generated eddy currents in the surrounding conducting structures and a resulting additional, unintended magnetic field. Taking these shim-to-shim interactions into account via calibration, it was demonstrated for the first time that the non-standard 3^{rd}-order SH terms enhanced B_0-field homogeneity in the human heart. However, they were attended by challenges for the shim system hardware employed in the presented work, which was indicated by the currents required to generate the optimal 3^{rd}-order SH terms exceeding the dynamic range of the corresponding shim coils. To facilitate dynamic shimming updated over the cardiac cycle for cine imaging, the benefit of adjusting the oscillating CPSS currents was found to be vital. The first in vivo application of the novel advanced B_0 shimming strategy mostly matched the simulations.

The presented technical developments are a basic requirement to quantitative and functional CMR imaging of the human heart at 7 T. They pave the way for numerous clinical studies about cardiac diseases, and continuative research on dedicated cardiac B_0 shimming, e.g., adapted passive shimming and multi-coil technologies.

Zusammenfassung

Herz-Kreislauf-Erkrankungen zählen zu den häufigsten Todesursachen weltweit und werden bisher in der Regel mittels Echokardiographie, Nuklearkardiologie und Katheterisierung untersucht. Die kardiale Magnetresonanztomographie hat das Potential diese invasiven Bildgebungsmodalitäten zu ersetzen. Dabei können sowohl das kardiovaskuläre System anhand der myokardialen Gewebestruktur sowie der Funktion und Perfusion des Herzens als auch Anatomie und Blutfluss der Koronararterien während einer einzigen Untersuchung charakterisiert werden. Im Gegensatz zu den weit verbreiteten klinischen Magnetresonanztomographie- (MRT) Geräten, welch häufig bei magnetischen Feldstärken zwischen 1.5 und 3T operieren, ermöglichen Feldstärken von 7 Tesla und mehr eine höhere Auflösung und somit eine akkuratere Quantifizierung kardialer Parameter.

Die Ultrahochfeld-Magnetresonanztomographie (UHF-MRT) ermöglicht einzigartige Einblicke in die Pathophysiologie des Herzens. Neuartige Kontrastmechanismen und die verbesserte Bildqualität leiden jedoch unter Inhomogenitäten des statischen magnetischen B_0-Feldes. Aufgrund der daraus resultierenden falschen räumlichen Registrierung der Voxel und einer Dephasierung des Signals innerhalb eines Voxels erzeugen diese Inhomogenitäten des B_0-Feldes eine Vielzahl unerwünschter Bildartefakte, beispielsweise eine künstliche Deformation des Bildes. Die resultierenden makroskopischen Gradienten führen zu Signalverlust und beeinträchtigen die Messung der effektiven transversalen T_2^*-Relaxationszeit, welche für die Charakterisierung myokardialen Gewebes essentiell ist. Vor allem bei der Bildakquisition mittels der *Steady State Free Precession* Methode führen Inhomogenitäten des B_0-Feldes zu Signalauslöschungen. Die dadurch entstehenden Bildartefakte erschweren die genaue Markierung des Myokards und haben so systematische Fehler bei der Bestimmung der kardialen Funktion zur Folge. Klinische MRT-Geräte sind dabei mit sogenannten Shim-Systemen ausgestattet um die Inhomogenitäten des B_0-Feldes zu korrigieren. Für die kardiale UHF-MRT des Herzens sind diese standardisierten Shim-Systeme allerdings nicht mehr ausreichend.

Im Fokus stand deshalb die Entwicklung moderner Methoden zur räumlichen und zeitlichen Korrektur der B_0-Inhomogenitäten, welche als „Shimming“ bezeichnet wird, für die kardiale UHF-MRT. Es wurde eine neue, herzphasen-spezifische Shimming-Strategie untersucht, welche auf der getriggerten Datenaufnahme, der Optimierung für die Anatomie des Herzens, sowie der kalibrierungsbasierten Modellierung des korrigierenden Magnetfeldes basierte. Zudem wurde der Einfluss technischer Limitationen der Hardware auf das Shimming, insbesondere das dynamische Shimming, in dieser Studie erörtert. Schließlich wurde die entwickelte neuartige Shimming-Strategie in vivo evaluiert, welche zu diesem Zeitpunkt die erste Implementierung einer herzspezifischen Shimming-Strategie in der humanen kardialen UHF-MRT darstellte.

Räumlich wies das B_0-Feld, welches im Rahmen dieser Studie im Herzen gemessen wurde, lokalisierte Inhomogenitäten im Myokardium auf. Diese variierten zudem in ihrer Größe sowie der Stärke der B_0-Inhomogenität zeitlich über den Herzzyklus hinweg und ließen sich mittels anatomisch angepasstem, kalibrierungsbasiertem Shimming deutlich reduzieren. Erzeugt man ein korrigierendes Magnetfeld mittels einer Shim-Spule, so werden jedoch Wirbelströme in nahen leitenden Strukturen und weiterhin ein zusätzliches, unerwünschtes Magnetfeld erzeugt. Berücksichtigt man diese Wechselwirkungen zwischen den verschiedenen Shim-Spulen, konnte erstmalig der Vorteil von korrigierenden Magnetfeldern in der Form von Kugelflächenfunktionen der dritten Ordnung für die kardiale UHF-MRT gezeigt werden. Hierbei waren jedoch die erforderlichen, besonders starken Ströme in den Shim-Spulen zu berücksichtigen, welche über den Herzzyklus hinweg oszillierten und für dynamisches Shimming angepasst werden sollten. Die erste in vivo Anwendung der neu entwickelten Shim-Strategie stimmte gut mit den vorigen Simulationen überein.

Die vorgestellten technischen Entwicklungen stellen grundlegende Anforderungen an die quantitative und funktionelle kardialer UHF-MRT dar. Klinische Studien zu kardialen Erkrankungen wie der Herzinsuffizienz erscheinen nun ebenso in Reichweite wie weitere Forschung zu kardialem B_0-Shimming basierend auf angepasstem passiven Shimming sowie Multikanal-Spulen.

Contents

Frequent abbreviations

Abbreviation	Description
ACT	acoustic cardiac triggering
B_0	static magnetic field
B_1	electromagnetic radiofrequency field
CMR	cardiac magnetic resonance
CPSS	cardiac phase-specific shimming
DL	deep learning
ECG	electrocardiogram
FA	flip angle
FID	free induction decay
FOV	field-of-view
γ	gyromagnetic ratio
G	magnetic field gradient
GRAPPA	generalized partially parallel acquisition
IQR	interquartile range
LA	long axis
LV	left ventricle
mGRE	multi-gradient-echo
MRI	magnetic resonance imaging
φ	signal phase
PD	proton density
pTx	parallel transmit
RF	radio-frequency
RV	right ventricle

Abbreviation	Description
RX	receive element
SA	short axis
SAR	specific absorption rate
SD	standard deviation
SH	spherical harmonics
SROI	shim-region-of-interest
SSFP	steady-state free precession
T	Tesla
TE	echo time
TR	repetition time
TX	transmit element
T_1	longitudinal relaxation time
T_2	transverse relaxation time
T_2^*	effective transverse relaxation time
UHF	ultra-high field
ω	Larmor frequency
χ_m	magnetic susceptibility

1 Introduction

A major cause of death worldwide is cardiovascular disease (1), which is typically diagnosed via echocardiography, nuclear cardiology, and catheterization as the gold standard techniques. These invasive imaging modalities could be replaced by cardiac magnetic resonance (CMR) imaging, which provides a "one-stop shop" solution for the characterization of the cardiovascular system - myocardial tissue structure, function and perfusion of the heart, as well as anatomy of and flow in the coronary arteries can all be measured in one imaging session (2,3). While 1.5 Tesla (T) or 3 T are standard field strengths for clinical magnetic resonance imaging (MRI) scanners, ultra-high field (UHF) MR systems are operated at 7 Tesla and above to potentially achieve a higher resolution and subsequent cardiac parameter quantification.

Unique insights into the pathophysiology of the heart are expected from UHF MRI, which offers enhanced image quality together with novel contrast mechanisms (4-6). These potential benefits of CMR imaging at 7 T are limited by inhomogeneities of the static magnetic (B_0) field. The myocardium, surrounding lungs, and blood possess different magnetic susceptibilities and, along with the curved shape of the heart, cause intricate B_0 field variations (7,8). These B_0-field inhomogeneities lead to spatial misregistration as well as intra-voxel dephasing and consequently to numerous unintended image artifacts, e.g., artificial image deformation (9). The induced macroscopic field gradients provoke signal loss due to truncated effective transverse relaxation times T_2^* (10). Extra temporal B_0 field alterations among diverse cardiac phases and breathing positions are due to cardiac and respiratory motion (11).

Modern CMR imaging methods used at clinical field strengths of 1.5 T and 3 T to estimate cardiac function comprise the cine technique, at which images are acquired at multiple heart phases assess cardiac motion and function, based on balanced steady-state free precision (SSFP) techniques (12). In SSFP-based pulse sequences, a rapid concatenation of radiofrequency (RF) pulses and time periods free of RF excitation alternate (13). One example is the balanced SSFP method, for which the overall moment of magnetic field gradients applied for imaging has to be equalized (14). This method is seriously affected by B_0-inhomogeneities, which cause signal drop-offs and result in banding artifacts in the

acquired images (15). The latter impede the accurate marking of the myocardium in CMR imaging at 3 T (12), and, inevitably, lead to systematic errors in cardiac function measurements. Due to the increased B_0-inhomogeneities in comparison to 3 T, SSFP-based imaging techniques are not widely used for CMR at 7 T yet. Numerous rapid pulse sequences, e.g., spirals (16) and echo-planar imaging (17), also do not very well tolerate inhomogeneous B_0-fields. In addition, a narrow B_0 field range is essential for designing optimized RF pulses, e.g., the parallel transmit (pTx) technique (18,19). These factors make B_0 field corrections essential to avoid artifacts in CMR imaging (20).

Up to now, B_0 inhomogeneities have been investigated for CMR applications at 1.5 T (21), 3 T (22), and 4 T (23). At UHF, the implementation of both an optimized saturation pulse train for human first-pass myocardial perfusion imaging (19) and the design of pTX RF pulses robust against respiration depend on a homogeneous B_0-field (11). Moreover, advanced shimming strategies tailored to CMR imaging methods, which have only been addressed for 1.5 T and 3 T (24), require additional technical improvements at 7 T. It is of interest whether the myocardial B_0-field inhomogeneities could be eliminated by shimming based on spherical harmonics (SH) functions or should be addressed by customized multi-coil hardware such as DYNAMITE (25,26).

In-depth knowledge of the higher, i.e., 3^{rd}-order and above, SH constituents of the magnetic field and their spatio-temporal evolution also plays a critical role for dynamic shimming applications (27-30). Moreover, it is useful for the design of non-Cartesian k-space trajectories (31,32), for which detailed knowledge about the B_0-field enables high-precision correction of the MR scanner's gradient system imperfections via waveform pre-emphasis based on the gradient system transfer function. When this technique is applied without the use of a dynamic field camera (33), a shortened T_2^* signal decay resulting from B_0-field inhomogeneities is a major limitation at 7 T (34). Accurately determined input response functions for gradients and shims (35,36), which could be derived precisely by employing a dynamic field camera (37), allow for the determination of optimal k-space trajectories and facilitate adequate pre-emphasis (38-40).

A prominent example for the above-mentioned non-Cartesian k-space trajectories are spiral trajectories, which were proven to be beneficial for imaging of the brain at UHF (41). Here, important advantages are the measurement of more k-space data points during

a single readout and reduced acquisition times in contrast to standard linear sampling (42-45). However, the images are prone to blurring resulting from B_0-field inhomogeneities (46). Spiral k-space trajectories were recently applied for cardiac real-time MRI using pre-emphasis at 3 T (33) and 7 T (47), where uncorrected B_0-field fluctuations were shown to limit the application of this technique at 7 T.

Therefore, the scope of this work included the quantification of spatial B_0-field fluctuations in the human heart as well as their temporal variation over the cardiac cycle. In a next step, the key factors influential on the B_0-field homogeneity were evaluated, which included the triggered B_0-map acquisition, the anatomy-matched shim-region-of-interest (SROI) selection, and calibration-based B_0-field modeling in dedicated shim software. Following the optimization of these individual steps, an advanced shim strategy was set up and the workflow was investigated via magnetic field simulations. Here, static shimming was carried out to identify the importance of specific SH shim terms and the consequences of hardware limitations. Moreover, dynamic shimming was examined to discover the benefits of CPSS, i.e., shimming dynamically updated on cardiac phases. Initial results of the in vivo implementation of the developed advanced shim strategy were presented, and benefits as well as drawbacks of the latter were discussed.

2 Theory

Major parts of the basic principles summarized hereafter consider common textbook knowledge, which is largely found in The Handbook of MRI pulse sequences (48), Magnetic resonance imaging: physical principles and sequence design (49), and In vivo NMR spectroscopy: principles and techniques (50). To preserve clearness, citations are only referred to where information goes beyond, in particular regarding the static magnetic B_0 field and its correction, i.e., shimming.

2.1 Spin polarization and relaxation

A nuclear spin located within a static magnetic B_0 field shows a quantum-mechanical behavior, which can be described by a Hamiltonian according to the literature:

$$\hat{H}_z = -\gamma\hbar B_0 \hat{I}_z \ . \tag{1}$$

In this case, the B_0 field directs to the z-direction of the coordinate system, and the z-component of the angular momentum operator $\hat{I}$ is represented by $\hat{I}_z$. $\hbar$ corresponds to the Planck's constant, and the gyromagnetic ratio is denoted by γ. Due to the angular momentum of a proton, known as the spin $\vec{I}$, a magnetic moment is induced:

$$\vec{\mu} = \gamma\hbar\vec{I} \ . \tag{2}$$

While a spin directing parallel to the B_0 field is referred to as *spin up* or ↑, a spin aligned with the anti-parallel direction is referred to as *spin down* or ↓. The resulting potential energy levels $E = -\mu \cdot B_0$ consequently split up, which is known as the Zeeman effect. For protons of spin $\pm\frac{1}{2}$, both states differ by $\Delta E = E_\downarrow - E_\uparrow = \gamma\hbar B_0$. Assuming an ensemble of non-interacting particles at the thermal equilibrium, the rate of corresponding

population probabilities $P_{\uparrow,\downarrow}$ accounts for $\frac{P_\downarrow}{P_\uparrow} = exp\left(\frac{\gamma\hbar B_0}{k_B T}\right)$. k_B denotes the Boltzmann constant, whereas T stands for the temperature. As a result, N spins feature the following macroscopic equilibrium magnetization or total magnetic moment $\vec{M}_0$:

$$\vec{M}_0 = N(P_\downarrow - P_\uparrow)\vec{\mu} = \frac{N\gamma^2\hbar^2}{4k_B T}\vec{B}_0 \quad . \tag{3}$$

The temporal evolution of the macroscopic magnetization $\vec{M}$ results from Liouville's equation and is straightforward connected to the B_0 field strength:

$$\frac{d}{dt}\vec{M} = -\gamma\vec{M} \times \vec{B}_0 \quad . \tag{4}$$

Deflected spins tend to restore the initial magnetization $\vec{M}_0$ via a relaxation process, which is described by the Bloch equations. The magnetization fraction M_z aligned with the B_0 field direction is characterized by the longitudinal relaxation time T_1, while the fraction $M_{x,y}$ perpendicular to the B_0 field is linked to the transversal relaxation time T_2:

$$\frac{d}{dt}M_z = -\gamma\left(\vec{M} \times \vec{B}_0\right)_z + \frac{M_0 - M_z}{T_1} \tag{5}$$

$$\frac{d}{dt}M_{x,y} = -\gamma\left(\vec{M} \times \vec{B}_0\right)_{x,y} + \frac{M_{x,y}}{T_2} \quad . \tag{6}$$

Hence, the temporal evolution of the three magnetization components is expressed as:

$$M_x = M_0 exp\left(-\frac{t}{T_2}\right) cos(\omega_0 t) \tag{7}$$

$$M_y = M_0 exp\left(-\frac{t}{T_2}\right) sin(\omega_0 t) \tag{8}$$

$$M_z = M_0\left[1 - exp\left(-\frac{t}{T_1}\right)\right] \quad . \tag{9}$$

Beside relaxation processes, the transversal magnetization $\vec{M}_{x,y}$ precedes around the B_0 field direction with the so-called Larmor frequency ω_0 according to the Bloch equations:

$$\omega_0 = 2\pi\nu_0 = \gamma B_0 \quad . \tag{10}$$

The transversal magnetization $\vec{M}_{x,y}$ induces a magnetic resonance (MR) signal, which has the shape of a free induction decay (FID), i.e., a damped sinusoidal function (Figure 1).

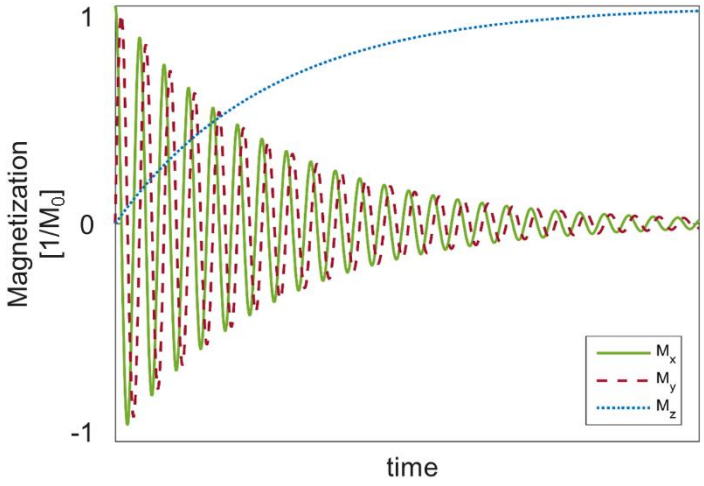

Figure 1. Relaxation processes for magnetization components due to the Bloch equations.

Local field variations ΔB_0 lead to decreased measurable transversal relaxation times T_2^*:

$$\frac{1}{T_2^*} = \frac{1}{T_2} + \gamma\Delta B_0 \quad . \tag{11}$$

The measurable radio-frequency (RF) induction signal, which is due to ω_0, results from the spin density distribution $\rho(\vec{r}, \nu)$ distinguished by locations $\vec{r}$ and frequencies ν:

$$s(t) = \iint \rho(\vec{r}, \nu) e^{-\frac{t}{T_2^*}} e^{2\pi i\nu t} d\vec{r} d\nu \quad . \tag{12}$$

The deflection of magnetization by a flip angle α and the generation of an induction signal $s(t)$ is achieved through an electromagnetic RF or B_1 field of a certain duration τ:

$$\alpha = \gamma \int_{t=0}^{\tau} B_1(t)dt \tag{13}$$

The complex B_1 field can be decomposed into two constituents: the fraction rotating clockwise is termed the B_1^+ field, and the fraction rotating counterclockwise the B_1^- field:

$$B_1^+ = \frac{B_{1,x} + iB_{1,y}}{2} \tag{14}$$

$$B_1^- = \frac{\left(B_{1,x} - iB_{1,y}\right)^*}{2} \tag{15}$$

The B_1^+ field is transmitted for signal excitation and interacts with the spins. Due to the reciprocity principle, B_1^- describes the field which induces the measurable MR signal $s(t)$ (51). In practice, RF coils consist of multiple transmit elements instead of a single loop or antenna. Optimal image quality is achieved by a homogeneous combination $B_{1,comb}^+(\vec{r})$, which superimposes the $B_{1,i}^+$ fields at position $\vec{r}$ of the $i = 1..n$ individual transmit elements with the complex signal amplitudes A:

$$B_{1,comb}^+(\vec{r}) = \sum_{i=1}^{n} A \cdot B_{1,i}^+(\vec{r}) \tag{16}$$

2.2 Image formation and pulse sequences

A constant Larmor frequency ω_0 across all observed spins does not provide insight into their spatial distribution. However, a spatial encoding of the measurable induction signal is realized by the application of magnetic field gradients, which could be generated across all three dimensions in a Cartesian coordinate system:

$$\vec{G}(\vec{r}) = \begin{pmatrix} G_x \\ G_y \\ G_z \end{pmatrix} = \begin{pmatrix} \partial B/\partial x \\ \partial B/\partial y \\ \partial B/\partial z \end{pmatrix} \quad . \tag{17}$$

G_x, G_y, and G_z are commonly created by dedicated gradient coils and superimposed to the static B_0 field. Thus, local B_0 field gradients $B_{0,loc}$ within the examined sample of spins are also encoded, which leads to a resulting Larmor frequency $\omega(x, y, z)$ of:

$$\omega(x, y, z) = \gamma\left(B_0 + xG_x + yG_y + zG_z + B_{0,loc}\right) \quad . \tag{18}$$

When magnetic field gradients are applied for a duration t, a spatially encoded induction signal is measurable – assuming an individual spin and negligible relaxation effects:

$$s(t) = s_0 e^{i\gamma \int_0^t \vec{G}(t)\vec{r}dt} \quad . \tag{19}$$

Subsequently, the k-space can be defined, which describes the local signal dependence generated by the magnetic field gradients $\vec{G}(t)$:

$$\vec{k} = \frac{\gamma}{2\pi} \int_0^t \vec{G}(t')dt' \quad . \tag{20}$$

For an entire spin density distribution $\rho(\vec{r})$ the measurable induction signal $s(\vec{k})$, which can successively be expressed through the k-space formalism, accounts for:

$$s(\vec{k}) = \int \rho(\vec{r}) e^{2\pi i \vec{k}\vec{r}} d\vec{r} \quad . \tag{21}$$

Here, both k-space and the underlying image space are linked by the Fourier transform:

$$\rho(\vec{r}) = \int s(\vec{k}) e^{-2\pi i \vec{k}\vec{r}} d\vec{k} \quad . \tag{22}$$

In practice, the k-space cannot be sampled continuously. Hence, data is acquired on a grid described by the corresponding discrete Fourier pair. Both its magnitude and phase encode specific information, at which the latter reveals the B_0 field. The number N of sampling steps and the field-of-view (FOV) define the spatial resolution by $\Delta x = \frac{FOV}{N}$. The entity of RF pulses and magnetic field gradients, which are applied to acquire data during an MR experiment, are referred to as pulse sequences. A common approach for sampling the k-space is the Cartesian trajectory, among which gradient echo-based (GRE) pulse sequences represent a major category and are explained successively (Figure 2).

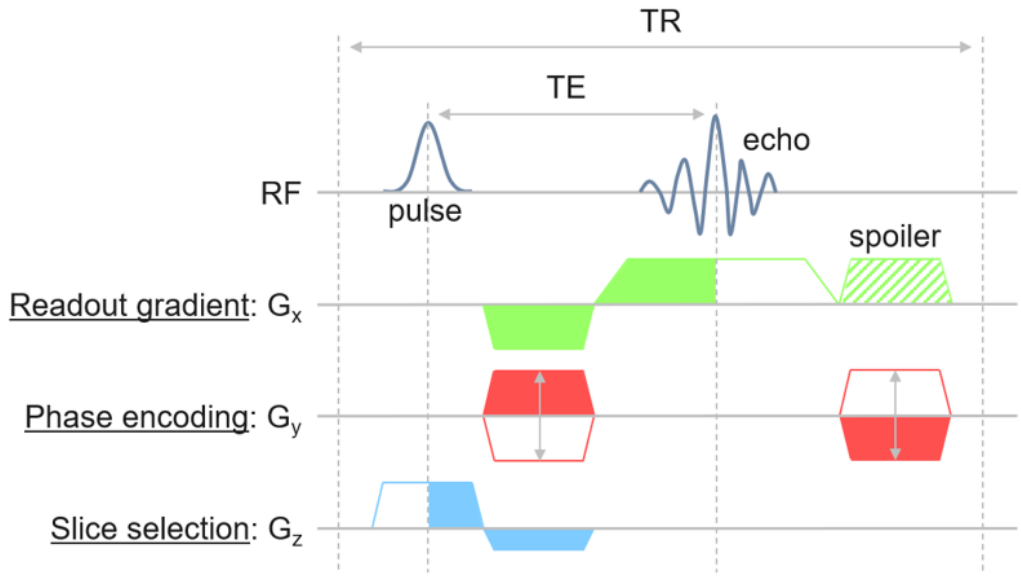

Figure 2. Schematic illustration of a gradient-recalled echo (GRE) pulse sequence.

A slice-selective magnetic field gradient G_z is applied during the RF pulse to only excite spins within the desired imaging plane. Note that unwanted dephasing caused by G_z is canceled via an appropriate gradient G_z of inverse polarity. To address a certain line in y-direction of the k-space, signal phase-encoding along this dimension is achieved by a

dedicated gradient G_y. To sample data points on this k-space line, a third gradient G_x, which creates a frequency dependency of the spins and is termed readout gradient, is applied along the x-direction. The occurrent spin dephasing is recalled by an upstream G_x gradient of inverse polarity. As a result, a so-called gradient-echo is observed at which image data is acquired. The time span between RF pulse and echo formation is known as the echo time TE. Before the next RF pulse is applied after the repetition time TR, another G_y gradient rewinds the signal phase. Spoiling gradients are applied after each TR cycle to minimize the remaining transversal magnetization.

2.3 B_0 field mapping and phase unwrapping

The data acquisition assumes a homogeneous B_0 field, while inhomogeneities cause local variations of ω_0. In general, a net magnetic induction $\vec{B}_{0,loc}$ occurs when an external magnetic field $\vec{H}$ interacts with a sample of spins. The spin magnetization $\vec{M}$, which denotes the total magnetic moment $\vec{m}$ per volume V, creates a magnetic induction of

$$\vec{B}_{0,loc} = \mu_0(\vec{H} + \vec{M}) \quad . \tag{23}$$

Here, μ_0 stands for the vacuum permeability. $\vec{M}$ depends on the magnetic susceptibility χ_m of a material, which describes the grade of magnetization within a magnetic field $\vec{H}$:

$$\vec{M} = \chi_m \vec{H} \quad . \tag{24}$$

$\chi_m < 0$ indicates diamagnetic materials, whereas substances with $\chi_m > 0$ are termed paramagnetic. $\chi_m \gg 1$ is characteristic for ferromagnetic materials. Due to Gauss's law, $\vec{\nabla}\vec{B} = 0$, there are no sources of the magnetic induction and $\vec{B}$ has to be perpendicular to interfaces. Significant discontinuities of χ_m consequently lead to strong B_0 field inhomogeneities prominent at air-tissue boundaries, e.g., the heart-lung interface inside the human body.

To obtain quantitative information about present inhomogeneities, the B_0 field has to be mapped across the shim-region-of-interest (SROI). This could be achieved using the Cartesian GRE pulse sequence, which allows data acquisition at multiple TE. Here, both an appropriate spacing of the TE to cover an adequately broad dynamic range of the MR signal, and a sufficiently large signal-to-noise ratio (SNR) at the longest TE are important. The SNR describes the ratio of the signal's mean and standard deviation. B_0 field maps can subsequently be computed from the accumulated phase $\Delta\varphi$ as its slope over TE:

$$\Delta B_0(x, y, z) = \frac{\Delta\varphi(x, y, z)}{\gamma \Delta TE} \quad . \tag{25}$$

B_0 mapping techniques can be divided into two major approaches, one-dimensional (1D) projection-based and three-dimensional (3D) volumetric methods. 1D projection-based techniques sense the B_0-field along particular orientations and provide the benefit of short acquisition time (52,53). Projection B_0-mapping is advantageous to derive the spherical harmonics (SH) constituents of local B_0-fields, which are sufficiently tackled with 1st- and 2nd-order SH shim fields in most cases (54). Across the whole heart, which represents a large FOV and consequent complex B_0 field distribution, 3D volumetric techniques are an appropriate tool. Here, B_0 field maps are calculated voxel-wise for the complete SROI. This approach is employed in typical shim software such as the *B0DETOX* application (26,55). In both cases, spatial and temporal phase wrapping has to be avoided and corrected where necessary.

A prerequisite for meaningful B_0 mapping is the proper unwrapping of the signal phase. Uncorrected phase-wraps namely result in discontinuities in the reconstructed B_0 maps, which are physically not plausible due to Maxwell's equations and limit their interpretability. Therefore, several methods exist to solve this issue. One option is the 3D *BEST PATH* algorithm (56). Quality maps, which are based on measures such as pseudo-correlation, phase derivative variance, or maximum gradient, are employed to unwrap highly reliable pixels first and less reliable pixels last. The 3D phase unwrapping paths are guided by the quality of the edges of the phase map. Another alternative is the phase region expanding labeler for unwrapping discrete estimates (*PRELUDE*) algorithm, which solves a cost function using a best-pair-first region merging approach (57). Phase

differences are penalized across boundaries. This algorithm is fast, automated, and applicable to arbitrary dimensions. For further improvement, the rapid open-source minimum spanning tree algorithm (*ROMEO*) has been introduced (58). Beside adapted measures for the quality maps and improved phase-unwrapping paths, single-step unwrapping can be performed across a fourth dimension, which enables temporal phase unwrapping across TE for B_0 mapping.

2.4 Calibration-based shim field modeling

B_0 field variations could be removed, i.e., shimmed, by the application of correcting magnetic fields of identical shape but opposite polarity. The standard approach in most MR systems is the generation of shim fields in the form of SH functions up to 2nd- or 3rd-order (Table 1). Here, the underlying room-temperature shim coils, which create the individual SH-shaped magnetic fields, are located around the magnet bore (59,60). The SH functions solve the Laplace equation $\Delta B_z = 0$ for the static magnetic field B_z aligned with the z-direction. B_z can subsequently be formulated as a linear combination of SH terms in spherical coordinates (61,62)

$$B_z(r, \varphi, \theta) = \sum_{n=0}^{\infty} \sum_{m=-n}^{n} C_n^m r^n P_n^m(\cos\theta) e^{im\varphi} \quad , \tag{26}$$

where the spherical position coordinates are expressed by r, θ, and φ. P_n^m represents the associated Legendre functions, which are of order *n* and degree *m*. Exemplary, all 1st- to 2nd-order SH terms as well as selected 3rd- (X3) and 4th-order (X4) terms are shown in along XY-, XZ, and YZ orientation in Figure 3.

Standard clinical scanners are equipped with 2nd-order SH shim coils, whereas state-of-the-art UHF MR systems offer correcting terms up to 3rd-order. 4th-order and above SH shim coils are up to now only integrated into research systems, e.g., by shim inserts (63). In any case, the shim coils influence each other via the generated magnetic fields.

Table 1. Spherical harmonics (SH) functions up to the 3rd-order. The SH terms are sorted by order and degree, and their abbreviation is assigned based on the dominating term in the Cartesian coordinates' formulation.

Order (n)	Degree (m)	Function	abbreviation
1	1	x	X
1	0	z	Z
1	-1	y	Y
2	2	$3(x^2 - y^2)$	X2-Y2
2	1	$3zx$	ZX
2	0	$z^2 - 1/2\,(x^2 + y^2)/2$	Z2
2	-1	$3zy$	ZY
2	-2	$6xy$	XY
3	3	$15x(x^2 - 3y^2)$	X3
3	2	$15z(x^2 - y^2)$	Z(X2-Y2)
3	1	$3/2\,x[4z^2 - (x^2 + y^2)]$	Z2X
3	0	$z[z^2 - 3/2\,(x^2 + y^2)]$	Z3
3	-1	$3/2\,y\big(4z^2 - (x^2 + y^2)\big)$	Z2Y
3	-2	$30xyz$	XYZ
3	-3	$-15y(y^2 - 3x^2)$	Y3

Shim-to-shim interactions provoke an individual treatment of each SH component and demand a shim system calibration to ensure a meaningful calculation of shim fields and appropriate currents (30). Moreover, the calibration procedure allows for an accurate determination of the total dynamic ranges, i.e., the maximum shim strength of each coil. The final calibration matrix *A* contains all information on the SH self- and cross-terms:

$$s = -I \cdot A^{-1} \quad . \tag{27}$$

A allows to derive the optimal shim settings s from the B_0-field before shimming with its SH components *I* and enables non-iterative single-step adjustments (62).

Beyond classical B_0 shimming based on SH functions, a number of advanced concepts for magnetic field modeling have recently been developed. A widely used approach is the dynamic multi-coil technique (DYNAMITE), where numerous shim coil loops are placed around the subject to generate B_0 field basis sets of much higher complexity than low-order SH functions (Figure 4) (25,26). Similar to SH-based shimming, the amplitudes C_n^m of the underlying non-orthogonal basis set of B_0 fields are determined for optimal homogeneity.

Moreover, the AC/DC approach drives individual elements of an RF receive coil array by DC currents (64). In this way, B_0 field homogeneity superior to 3rd-order SH shimming could be achieved. The integrated parallel reception, excitation, and shimming (iPRES) technique also combines both RF and B_0 shimming technology (65). Since arranging the shim coils in the same localized setup is complicated for CMR measurements due to different body shapes and sizes, only SH-based B_0 shimming is considered in this work. Multi-coil hardware for CMR imaging may be investigated in future studies.

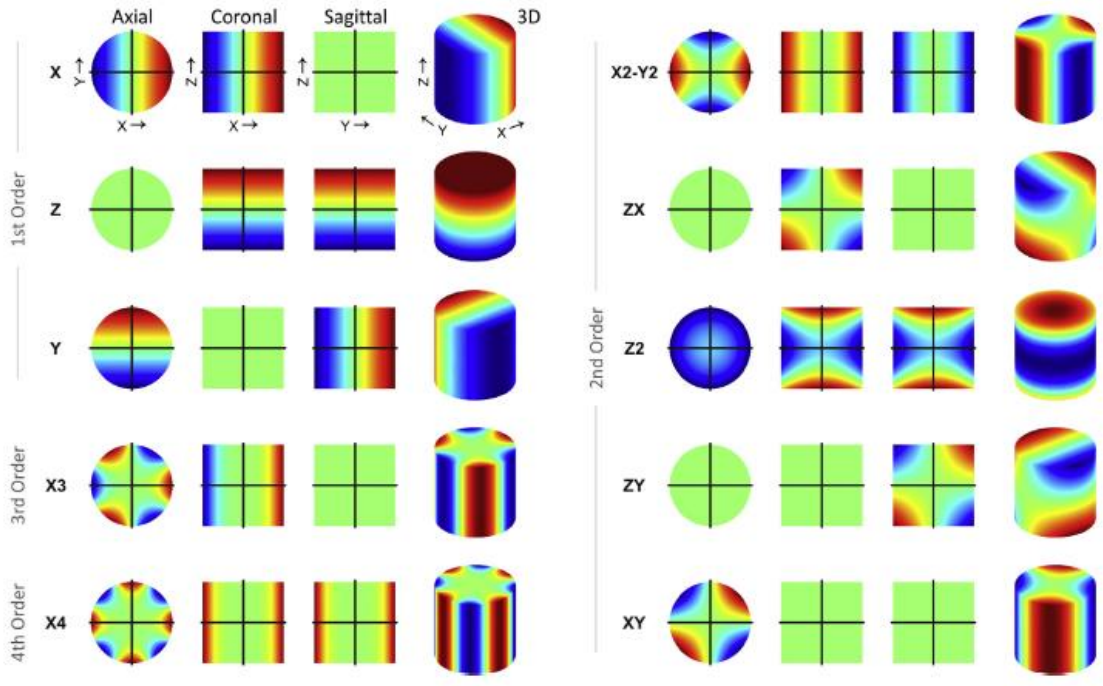

Figure 3. Schematic illustration of SH functions. Shown are all 1st- and 2nd-order together with selected 3rd- and 4th-order terms on a cylindrical volume, which represents the typical case inside the bore of an MR system. Adapted with permission from Reference (66).

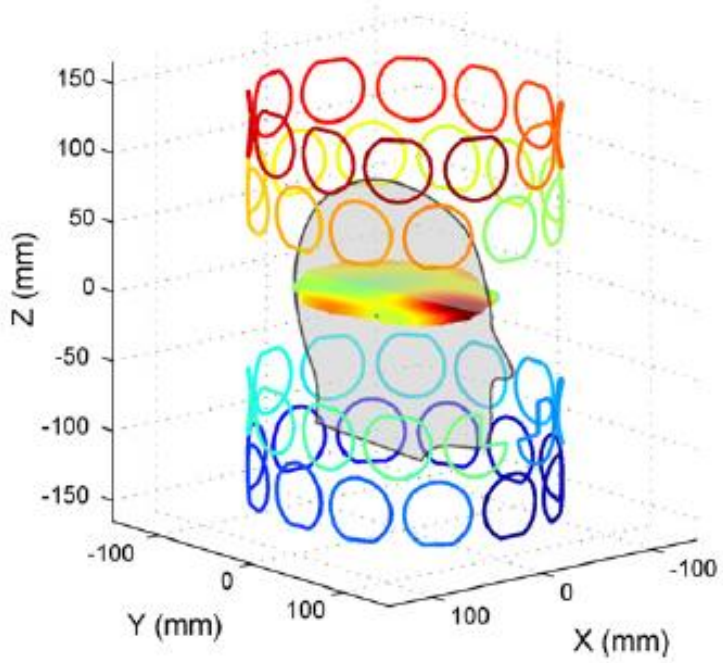

Figure 4. Dynamic multi-coil technique for B_0 shimming of the human brain. In the setup shown above 48 individual shim coil loops are arranged in four rows to correct the measured B_0 field distribution. Adapted with permission from Reference (26).

2.5 Anatomy and function of the human heart

When CMR image and B_0 field data are acquired, several specialties have to be taken into account due to the shape of the heart as well as its function. Major aspects include double-oblique slice orientations to accurately determine volumetric parameters and the need for triggering because of cardiac motion, both of which are elucidated hereafter.

In general, the heart is the muscular pump for blood circulation in the systemic and the pulmonary system. The left-sided chambers split into the left atrium and the left ventricle with the aorta as its outlet. The left-sided muscle, e.g., the myocardium, is the driving force for the systemic circulation, distributing highly oxygenated blood through the body. The right-sided chambers split into the right atrium and the right ventricle, which are part of the pulmonary system and use the truncus pulmonalis as outlet (Figure 5).

To characterize the anatomy of the heart and cardiac function with CMR, the common image orientations are on the one hand the long-axis (LA) view, in which both the left and right ventricles and atria are visible similar to Figure 5. And on the other hand, the so-called short-axis (SA) view covers ventricular imaging slices perpendicular to the septum to properly monitor the contraction and expansion of the myocardium.

The right-ventricular myocardium fulfills the function of circulating the oxygen-deficient blood throughout the lungs to the left heart. Left and right ventricle are separated by the interventricular septum, while the left and right atria are separated by the interatrial septum. The atria and ventricles are divided by the mitral valve on the left side, and the tricuspid valve on the right side. In conjunction with the myocardial contraction, the aortic and pulmonary valves are opened, while the mitral and tricuspid valve are closed, which regulate and direct the circulation of the blood. The cardiac contractions follow a rhythmic sequence of contraction (systole) and relaxation (diastole) of the myocardium, allowing for ventricular filling before the next contraction. This temporal evolution forms the electrocardiogram (ECG).

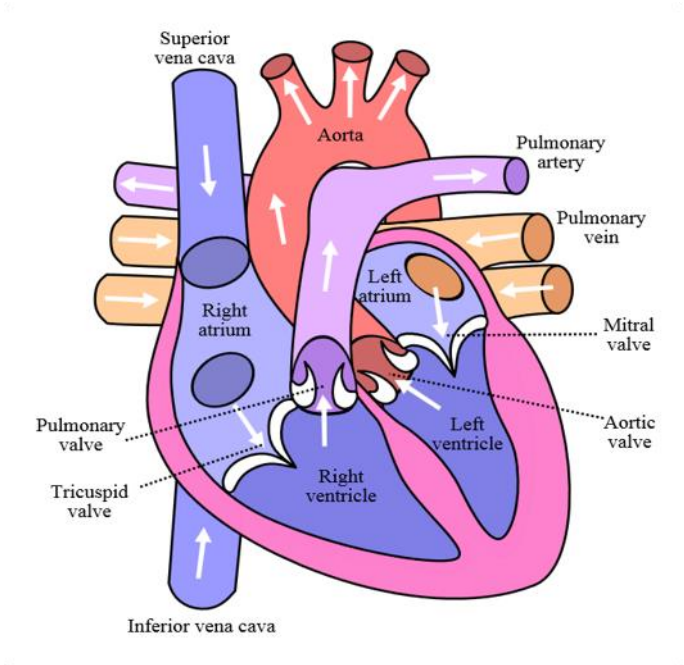

Figure 5. Schematic illustration of the human heart. Adapted from Reference (67).

The electric activation is initiated at the sinus node, which is the impulse generator of the heartbeat and determines the heart rate. The activation moves on through the atria, which contract at the same time and pump the blood into the heart chambers. In the ECG, this correlates to the P wave (Figure 6). Afterwards the electrical excitation reaches the atrioventricular node, acting as a gatekeeper between atria and ventricles for the electrical activation, which then is distributed throughout the ventricular electrical conduction system. As a consequence, both chambers contract, which is indicated by a large spike termed the QRS complex of the ECG. In a final step, both ventricles relax again, which is represented by the T wave. The most distinct feature of the ECG is the pronounced R wave, which is consequently selected as the trigger signal. Due to the slow cardiac motion in diastole, image data is often acquired during this cardiac phase to reduce motion artifacts.

The interaction with electromagnetic fields generated by the gradient system and the liability to the magnetohydrodynamic effect form limitations of the ECG. In contrast, another technique called acoustic cardiac triggering (ACT) addresses the phonocardiogram. The first heart tone, which results from the systolic closure of the atrioventricular valves, is traced here. The trigger signal quality relies on accurate positioning of the stethoscope and could be disturbed by potential patient breathing and tentative background noise. These findings were demonstrated in an earlier study, where ACT was checked against vector ECG and pulse oximetry triggering (68).

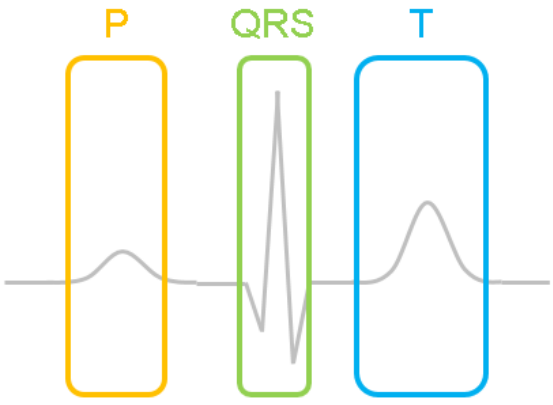

Figure 6. Schematic illustration of the electrocardiogram (ECG) of the human heart.

3 Methods

3.1 Experimental setup

All data acquisition was carried out on a 7T whole-body MR scanner (MAGNETOM™ *Terra*, Siemens Healthineers, Erlangen, Germany), which is visualized in Figure 7. The magnet itself, which had a bore diameter of 60 cm, was cooled by the "Zero Helium boil-off" technology. In this way, minimum evaporation of helium was enabled (69). The 7T MR scanner was equipped with a gradient system capable of creating a maximum strength of 80 mT/m and a slew rate of 200 T/m/s. In comparison to 3T MR scanners, the SNR was doubled, and an in-plane resolution of 0.2 mm could be achieved for neurological applications (70). Up to 64 channels are available for RF signal receive coils. It has to be noted that this 7T *Terra* MR scanner has only been cleared for neurological and musculoskeletal clinical surveys by the US Food and Drug Administration (FDA) up to now (71). Examinations of the heart were only allowed for dedicated research purposes.

Figure 7. 7T *Terra* whole-body MR scanner for conducting *in vivo* experiments in human volunteers, patients, and large animals. The MR scanner, which was installed at the Comprehensive Heart Failure Center (CHFC) as part of the University Hospital Würzburg, facilitated state-of-the-art technologies such as parallel signal transmission.

At the beginning, the *in vivo* image acquisition on the 7T *Terra* MR scanner was performed with a commercial single-channel transmit (1Tx) / sixteen-channel receive (16Rx) RF coil (MRI Tools, Berlin, Germany). The modular RF coil design, which was tailored to the human thorax, consisted of an anterior and posterior part (Figure 8A). The limitation to 1Tx signal transmission was a significant drawback, which prevented the implementation of B_1^+ shimming to improve the transmit field homogeneity. At 7 T, initial results demonstrated that B_1^+ shimming improved the SNR along with line profiles across the heart (4).

To homogenize the B_1^+ field in an optimal way, a new RF coil capable of parallel transmission (pTx) was developed (Figure 8B), which employed eight elements for signal transmission (8Tx) and sixteen for reception (16 Rx). B_1^+ shimming via adjustment of the signal phases for all transmit elements is challenging due to energy deposition constraints. Therefore, electromagnetic simulations were conducted for the human body models *Duke* and *Ella* (IT'IS Foundation, Zurich, Switzerland) in *CST Microwave Studio* (Computer Simulation Technology AG, Darmstadt, Germany) to account for safety aspects. The final product version enabled image quality superior to the commercial RF coil (72,73).

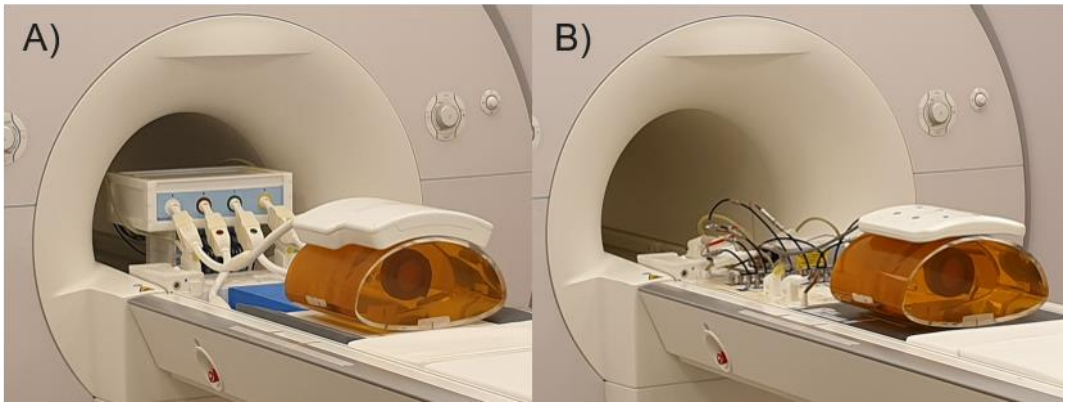

Figure 8. Radio-frequency coils for *in vivo* CMR of the human heart. The commercial RF coil operated only in single-channel transmit (1Tx) mode (A). In contrast, the new RF coil enabled parallel transmission (pTx) and allows for an optimization of the $\boldsymbol{B_1^+}$ field homogeneity (B). $\boldsymbol{B_1^+}$ shimming was realized by manipulation of the signal amplitude and phase for each transmit element.

Throughout all *in vivo* human examinations, two cardiac monitoring techniques were applied to continuously keep track of cardiac activity (74). The functionality of both techniques and related hardware devices, namely the scanner-integrated electrocardiogram (ECG) and an acoustic cardiac triggering (ACT) system (EasyACT, MRI Tools), has already been described in Section 2.5 (Figure 9).

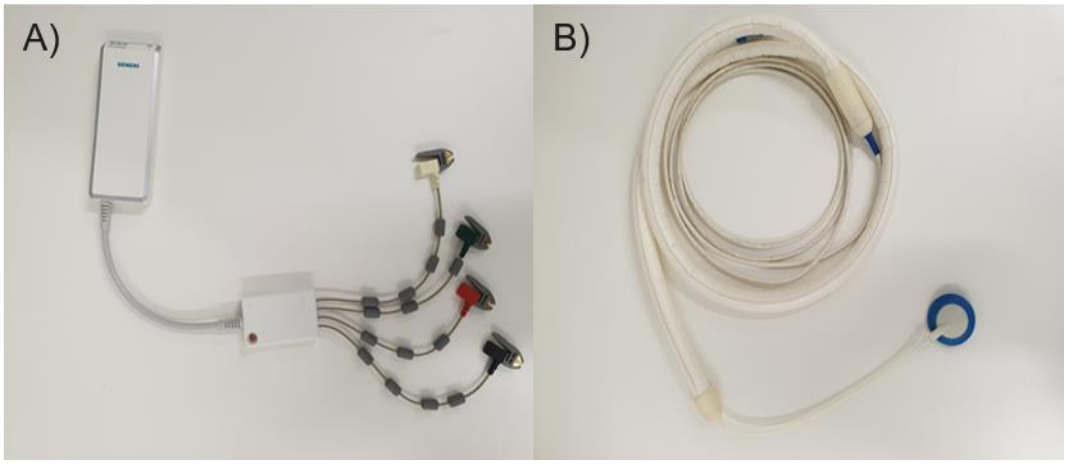

Figure 9. Hardware devices for applied cardiac triggering techniques. The ECG device addressed the electrocardiogram (A), whereas ACT employed the phonocardiogram (B).

3.2 Spatio-temporal B_0 variations

3.2.1 B_0-field measurements

This study was approved by the Ethics Committee of the University of Würzburg (7/17-sc). Ten healthy humans volunteered to be scanned for this project and gave their written informed consent. A training group was set up of four subjects to assemble an imaging protocol for the quantification of spatio-temporal B_0 field variations. The imaging protocol was carried out for the study group of additional six subjects (3 female, 3 male), who were 23.7 ± 2.7 years old, had a weight of 73.5 ± 15.4 kg, and a height of 176.5 ± 9.4 cm.

Spatial B_0 field distributions across the heart were acquired at a trigger delay of 490 ± 66 ms during mid-diastole with the following sequence settings: TE1/TE2/TE3/TE4/TE5 = 1.7/2.8/4.0/6.0/9.7 ms, TR = 401 ms, matrix = 128 × 128, FOV = 300 × 300 mm^2, number of slices = 3, slice thickness = 6.0 mm, slice separation = 1.2 mm, flip angle = 25°, GRAPPA = 3, and number of segments = 29. A typical breath-hold duration of 15 seconds allowed for the measurement of three transversal mid-ventricular slices.

To measure the temporal B_0 field fluctuations over various cardiac phases, several sequence parameters such as TR and number of TEs had to be modified. The eight cardiac phases, at which the field map data were acquired, were equally distributed over an RR interval of 970 ± 127 ms. The following parameters were set: TE1/TE2/TE3 = 1.7/2.8/4.0 ms, TR = 90 ms, matrix = 128 × 128, FOV = 320 × 320 mm^2, number of slices = 3, slice thickness = 6.0 mm, slice separation = 1.2 mm, flip angle = 40°, GRAPPA = 3, and number of segments = 15. Note that the data for each slice was measured in an individual breath-hold of 15 seconds net time.

3.2.2 Evaluation of B_0 maps

At first, the B_0 maps were reconstructed from the measured field map data by voxel-wise linear regression of the signal phase evolution over echo time according to Section 2.3. Spatial phase-unwrapping was performed using the PRELUDE algorithm of the FMRIB Software Library (FSL) from the Oxford Center for Functional MRI of the Brain (57,75), which was relatively robust and considered the gold standard (76). It has to be noted that the B_0 maps were calculated in *B0DETOX* and then exported from the shim software.

Afterwards, the standard deviations (SD) and interquartile ranges (IQR) of the spatial magnetic field distributions were computed for the manually segmented regions-of-interest in *MATLAB* R2015b (MathWorks Inc, Natick, MA, USA). For both the left- and right-ventricular myocardium, the temporal B_0 field fluctuations were obtained as the differences ΔSD and ΔIQR between systolic and diastolic field map data. In detail, the 25^{th} and 75^{th} percentiles of the B_0 distribution allowed for a quantification of the IQR.

3.3 Heart-specific B_0 shim strategy

3.3.1 Shim-region-of-interest selection

The 7T MR scanner used in this work featured a partial 3rd-order SH shim system, allowing for B_0-shimming beyond 1st- to 2nd-order SH terms. The built-in hardware enabled the generation of the 3rd-order SH terms Z3, Z2X, Z2Y, and Z(X2-Y2). Shim coils for magnetic field modeling based on the X3, Y3, and XYZ functions were not integrated. To generate a uniform B_0 field inside the heart using the shim system at hand, a precise SROI selection was proven to be beneficial (12,77). Thus, three approaches based on a transversal SROI cuboid using the vendor-supplied shimming platform were compared: (i) volume-selective shimming covering the whole heart, (ii) slab-selective shimming of the three acquired slices, and (iii) slice-selective shimming of merely the central slice. Beyond this, no other anatomy-matched SROI adjustment was feasible. The vendor-supplied B_0 mapping was executed without cardiac triggering and in exhaled breath-hold position, while making use of the shortest available first TE and inter-echo spacing. The pulse sequence featured the following default parameters (78): TE1/TE2 = 1.02/3.06 ms, TR = 4.3 ms, matrix = 64 × 64, FOV = 282 × 282 mm^2, number of slices = 52, slice thickness = 4.4 mm, slice separation = 0.9 mm, flip angle = 4°, GRAPPA = 2, and number of segments = 1.

3.3.2 Calibration of spherical harmonics shim system

A careful system calibration is a requirement to determine the total dynamic range of each SH shim term and essential cross-term corrections. For this purpose, an experiment using a spherical oil phantom and a 1TX / 2RX birdcage coil (Siemens Healthineers) was set up (79). Each shim term was modified in seven steps, which utilized 10% of the dynamic range for the linear gradients, and 30% to 50% for the higher orders, relative to a reference B_0 map. The parameter settings for the pulse sequence were: TE1/TE2/TE3/TE4 = 1.0/1.3/2.0/4.0 ms, TR = 30 ms, matrix = 108 × 128, FOV = 186 × 220 mm^2, number of slices = 64, slice thickness = 2.7 mm, and flip angle = 25°.

After reconstructing the B_0 field maps, the underlying SH components were derived from the computed magnetic field distributions. The calculation of the adequate shim fields, i.e., each SH constituent in inverse polarity, was performed by constrained least-squares fitting (9,80). Compared to other constrained nonlinear optimization methods, the applied Levenberg-Marquardt algorithm was found to be most resilient against changes in starting point values (81). The limited dynamic ranges of the shim coils could then be accounted for in the optimization process. In other words, the shim field was regularized to the hardware capabilities. Based on the determined SH components in the reconstructed B_0 map, a shim field and corresponding shim currents were computed. All magnetic field modeling steps could be performed in the *B0DETOX* software environment.

3.3.3 Simulation of static shimming

The spatial pattern of B_0 field variations was addressed on B_0 maps at a mid-diastolic cardiac phase, which minimized the influence of cardiac motion due to ventricle contraction during systole (18). Regarding the correction of the SH components present in the measured B_0 fields, it was investigated whether the dynamic range of each shim coil was adequate to balance the respective SH term. This task was achieved by not restricting the currents for the least-squares optimization during B_0 field shaping. Beyond, three kinds of shims were simulated to analyze the impact of the 3^{rd}-order terms: 2^{nd}-order only, 2^{nd}- plus 3^{rd}-order incorporating hardware restrictions, and 2^{nd}- plus 3^{rd}-order neglecting those restrictions. In each case, the un-shimmed B_0 field served as the input to simulate the specific shim. The term un-shimmed refers to the system's default shim settings, which employed less than 5% of the maximum current in all shim coils.

3.3.4 Simulation of dynamic shimming

For eight equally-spaced phases of the cardiac cycle the B_0 field in the heart was monitored to resolve temporal shim field variations. The dynamic alterations of required shim currents were determined by the anatomy-matched SROI selection and calculation

of correcting magnetic fields for each cardiac phase. Since the MR system at hand was not provided with the hardware essential for cardiac phase-specific shimming (CPSS), it was investigated whether an averaged static shim, which facilitated the mean of all eight CPSS fields, would be beneficial for applications such as cine imaging.

3.3.5 Advanced in vivo B_0 shimming

The previous findings paved the way for an advanced shim strategy, which was then made available for *in vivo* shimming and comprises of the following procedure (82,83):

1. B_0 maps were measured for three slices at a mid-diastolic cardiac phase in a triggered fashion with ACT;
2. The anatomy-matched SROI adjustment was carried out by hand on the magnitude images for all slices together with a voxel-specific field-gradient boundary value to eliminate outliers;
3. SH-based magnetic field optimization was performed in the *B0DETOX* software environment and the derived shim fields in Hz/cm^n, where n denotes the order of the SH components, were converted to shim coil currents units;
4. The calculated shim coil currents were employed on the MR system, and step 1 was iterated to validate the derived B_0 field.

The acquired field map data were copied from the MR system to a dedicated computer for data analysis and imported into the *B0DETOX* software environment. The reconstruction of field map data was executed as delineated in Section 2.3, and the anatomy-matched SROI was subsequently traced by the user on the magnitude images. In the next step, the optimal shim fields and underlying currents were calculated as specified in Section 2.4. The obtained hardware settings, which generated the correcting B_0 field, were saved as a text file and applied to the MR system via a batch script. The entire procedure required approximately 6-8 minutes, in which most of the time was needed for the adjustment of the anatomy-matched SROI by the user and the generation of the derived shim fields via setting of the currents on the scanner console.

The initial B_0-field maps, which were acquired as the basis for the shim field computations, were then checked against those measured after the application of these shim fields with regard to homogeneity. For this purpose, the SDs of the B_0-field within the heart were calculated as a comparative measure.

4 Results

The investigations on B_0 shimming of the human heart, including the analysis of spatio-temporal B_0 field variations as well as static and dynamic cardiac phase-specific shimming, are published to some extent in (84).

4.1 Spatio-temporal B_0 variations

Figure 10 displays the spatial B_0-field distribution in both LA and SA views. Severe negative B_0-field variations were present near the apex in the LA view. Beyond that, strong B_0-field variations were found at the anterior and posterior wall of the left-ventricular myocardium in the SA view. A segment-wise histogram analysis revealed that the -100 Hz to 100 Hz interval covers most data points. However, localized spots of exceptional values were found in the left- and right-ventricular myocardium (Figure 11).

Temporal variations of the B_0 field in the myocardium were observed over the cardiac cycle (Figure 12). In addition, a slice-to-slice variation of the ΔSD in the left-ventricular myocardium arose. A mean ΔSD of 10 ± 5 Hz and ΔIQR of 19 ± 12 Hz between systole and diastole, for which cardiac phases similar to subject 3 were monitored, were found for all slices and subjects. The right-ventricular ΔSD added up to 17 ± 9 Hz and ΔIQR to 17 ± 10 Hz averaged over all slices and subjects. Considering the septum, which is exemplary highlighted in Figure 11C (segment 4), a temporal B_0-field fluctuation of ΔSD_{Sep} = 3 ± 2 Hz was measured. As a result, the smallest ΔSD and ΔIQR occurred in the septum in comparison to both ventricles. Center frequency changes yielded $\Delta F_{0,LV}$ = 8 ± 6 Hz and $\Delta F_{0,RV}$ = 16 ± 11 Hz averaged over all subjects and slices.

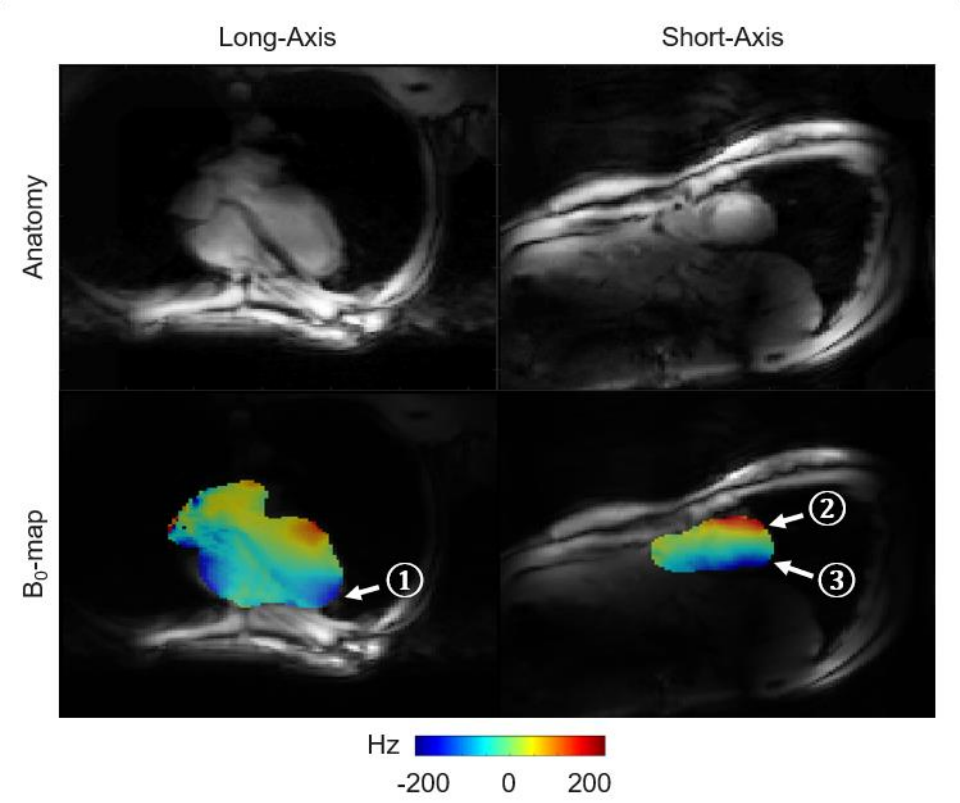

Figure 10. B_0 field distribution inside the human heart in standard anatomical views. Distinct negative B_0-field inhomogeneities are present near the apex in the long-axis (LA) view (1). Precise B_0-field variations were also found at the anterior (2) and posterior (3) wall of the left-ventricular myocardium in the short-axis (SA) view. The contrast of the anatomical images was modified for visualization, employing the "adapthisteq" *MATLAB* function, which executes contrast-limited adaptive histogram equalization. Adapted from Reference (84).

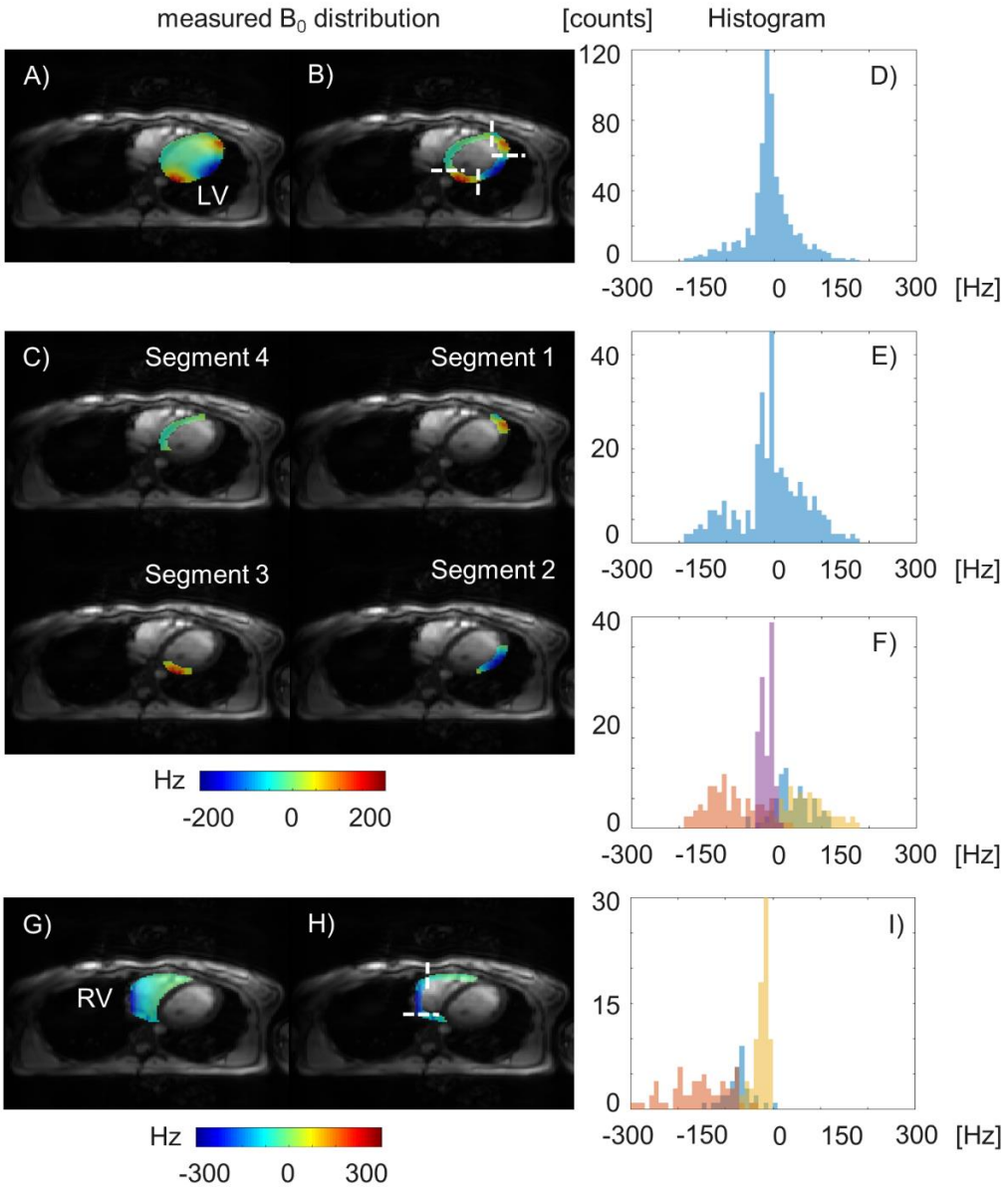

Figure 11. Spatial B_0-field distribution across the heart. Displayed are the calculated B_0 distributions (left) and underlying histograms (right) for the whole left ventricle (A), the left-ventricular myocardium (B), and four segments of the latter (C). The histograms D-F correlate with the measured B_0 distributions A-C at a time. In F, the color blue represents segment 1, red segment 2, yellow segment 3, and purple segment 4. The B_0 distribution across the entire right ventricle is visualized in G. Once more, the B_0 field variations in the myocardium (H) are highly relevant and visualized in histogram I. In I, the color yellow correlates with the anterior segment in H, blue with the inferior segment, and red with the lateral segment. Adapted from Reference (84).

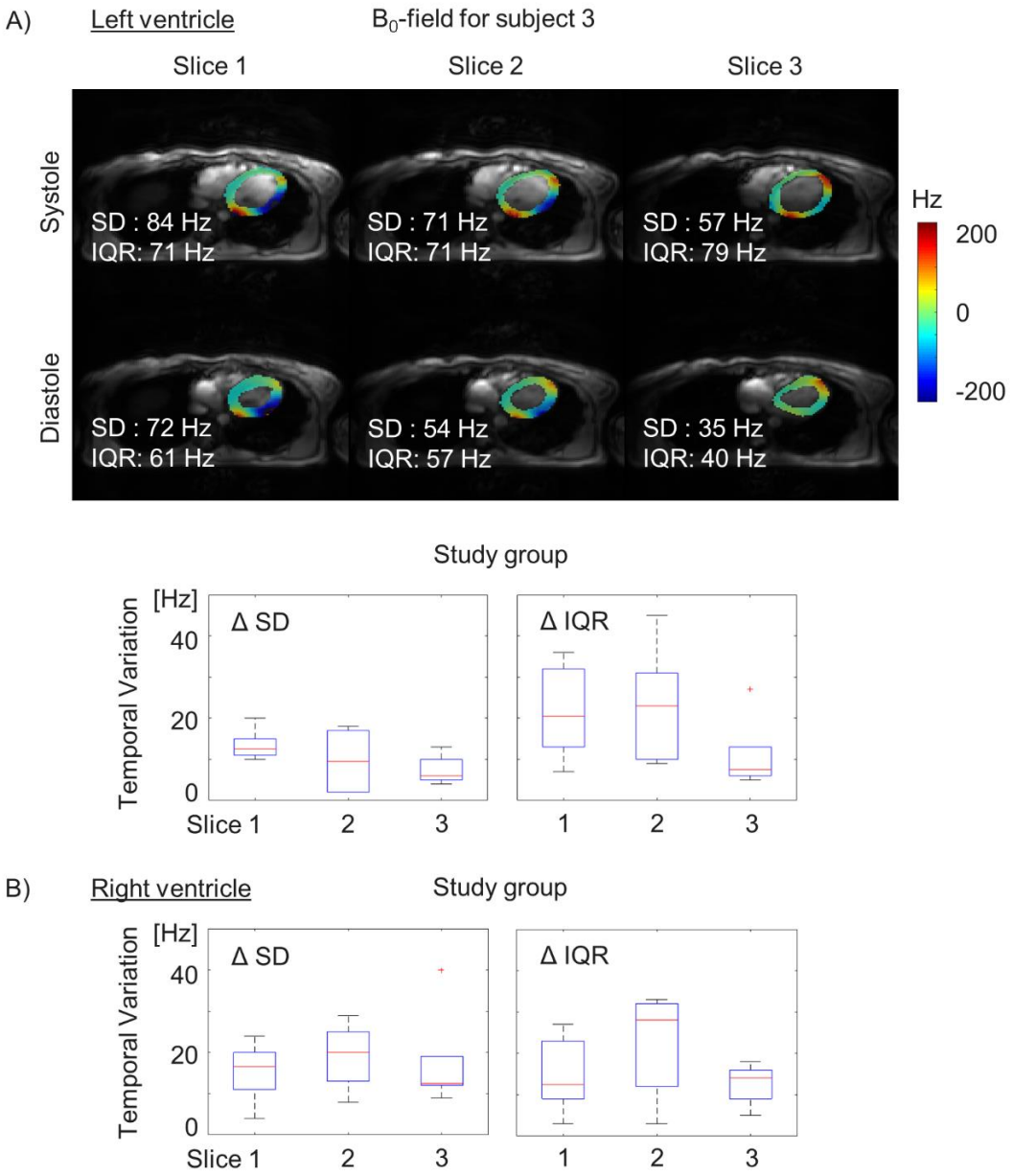

Figure 12. Temporal B_0-field variation in the myocardium over the cardiac cycle. The left- (A) and right-ventricular myocardium (B) were opted for analog to Figure 11B and Figure 11H. The differences ΔSD and ΔIQR between B_0-field distributions in (B), which were computed for the same systolic and diastolic cardiac phases as displayed in (A), are summarized for all study group subjects in box plots. Here, the red line markers delineate the median, and the blue line markers illustrate the 25th and 75th percentiles. The black line markers correspond to the most extreme data points not considered outliers, and outliers are visualized as a red '+'. Note that volume-selective shimming was performed prior to the B_0 map acquisition. Adapted from Reference (84).

4.2 Evaluation of heart-specific B_0 shim strategy

4.2.1 Shim-region-of-interest selection

After application of the volume-, slab-, and slice-selective shimming, B_0 maps were acquired in each case to evaluate the three SROI selections (Figure 13).

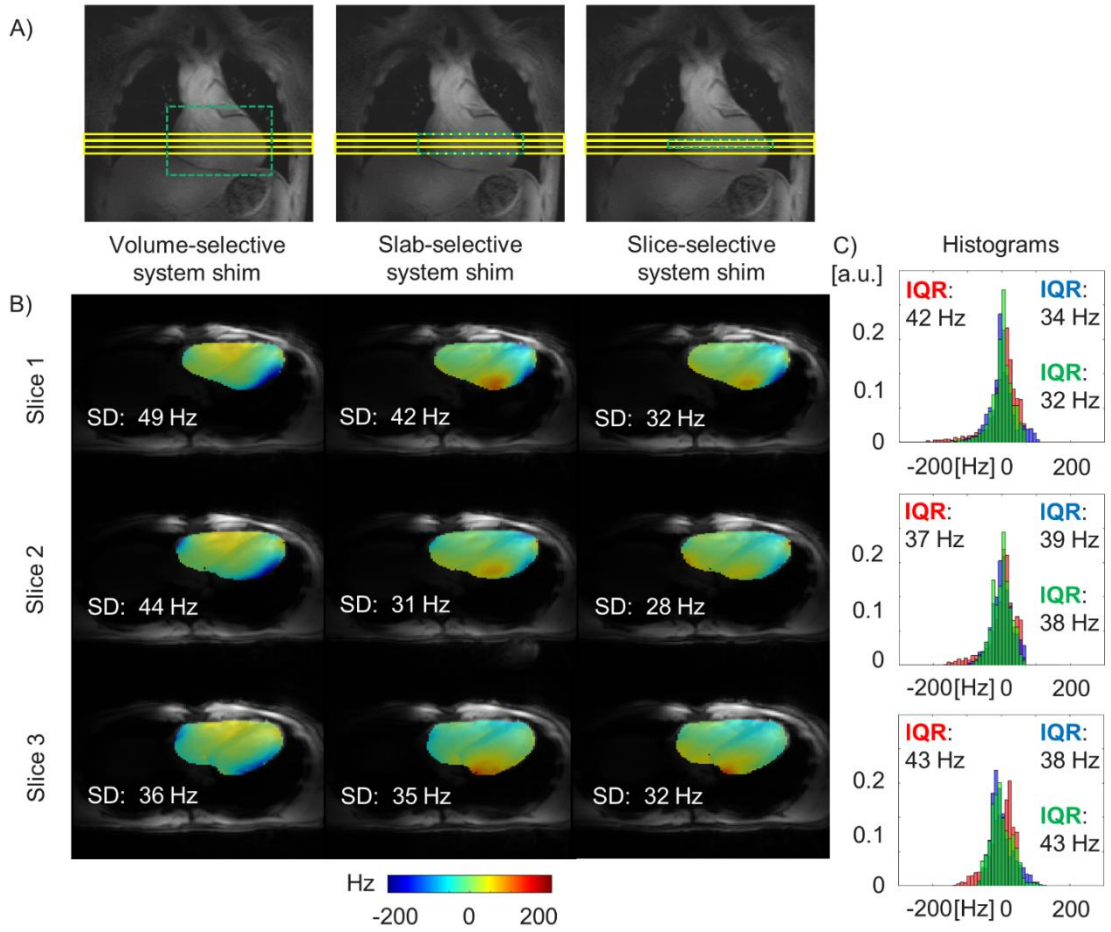

Figure 13. Adjustment of the shim-region-of-interest (SROI). The adaption of the SROI cuboid is visualized for the vendor-supplied volume-, slab-, and slice-selective shimming (A). In each case, the SROI covered the entire heart, but as less parts of circumjacent organs as feasible in-plane. Exemplary, (B) shows the acquired B_0 distribution for subject 7 in conjunction with the respective histograms in (C) gained after the volume- (red bins), slab- (blue), and slice-selective shimming (green). Adapted from Reference (84).

The slab-selective shimming led to a decreased SD and IQR in all three measured slices, implying a more homogeneous B_0 distribution. Quantitatively, the slab-selective shimming reduced the SD of the B_0 distribution in the central slices by 13 ± 6 Hz and (26 ± 11) % versus the volume-selective shimming across all study group subjects (Table 2). However, the insight delivered by Table 2 unveiled that slice-selective shimming reduced this value further for no more than two subjects.

Table 2. Comparison of different vendor-supplied shimming procedures. The field homogeneity is quantified by the standard deviations (SD) of B_0 distributions at a mid-diastolic cardiac phase as exemplary demonstrated for subject 7 in Figure 13. Note that the SDs are provided for the central slices of the three-slice stack through the heart. The last row presents the mean value SD across all subjects

Subject	Volume-selective shimming SD (Hz)	Slab-selective shimming SD (Hz)	Slice-selective shimming SD (Hz)
5	42	32	39
6	49	28	54
7	44	31	28
8	66	46	42
9	49	45	49
10	51	39	45
	50 ± 8	37 ± 7	43 ± 8

4.2.2 Calibration of spherical harmonics shim system

An individual step of appropriate B_0 mapping of a certain underlying shim field is summarized in Figure 14 for the spherical oil phantom experiment. The static magnetic field reconstruction was based on linear regression of the signal phase evolution over four different TE values and computed voxel-by-voxel. The complete calibration routine for a specific shim component, which in this case was the SH term Z(X2-Y2), is demonstrated in Figure 15. All corresponding generated cross-terms are given in Figure 16.

For all SH terms the entire calibration procedure visualized in Figure 15 and Figure 16 was repeated. The total dynamic range of each shim coil was: X = 2124 Hz/cm, Y = 2120 Hz/cm, Z = 2129 Hz/cm, X2-Y2 = 6.1 Hz/cm^2, ZX = 12.6 Hz/cm^2, Z2 = 40.2 Hz /cm^2, ZY = 12.3 Hz/cm^2, XY = 6.2 Hz/cm^2, Z(X2-Y2) = 0.10 Hz/cm^3, Z2X = 0.35 Hz/cm^3, Z3 = 0.68 Hz/cm^3, Z2Y = 0.34 Hz/cm^3. Figure 17 provides the entire final calibration matrix. Note that the observed shim-to-shim interactions between 3rd- and 1st-order SH terms were eminent, whereas they were less prominent but still not negligible between 3rd- and 2nd-order as well as 2nd- and 1st-order terms.

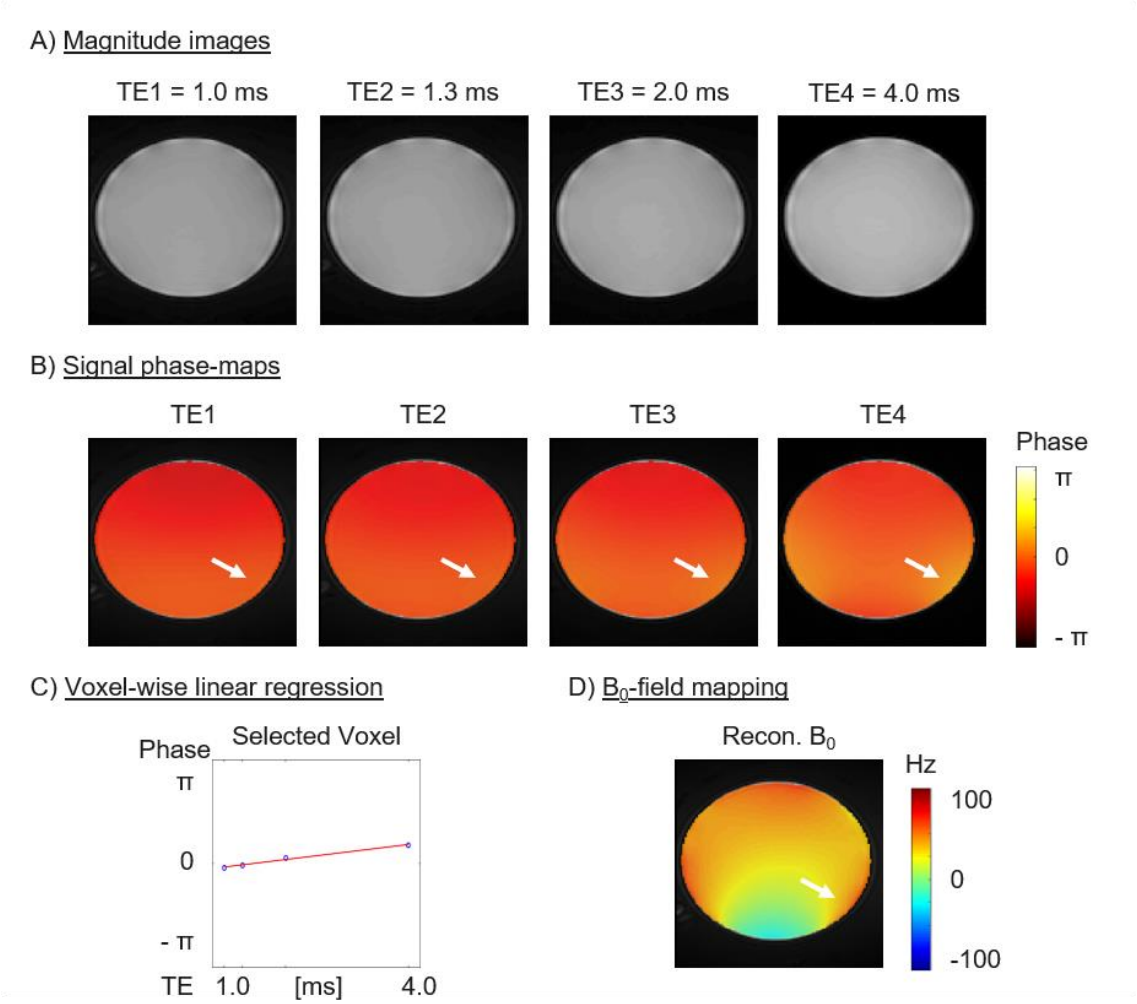

Figure 14. B_0 field mapping based on the phase evolution over multiple echo times (TE). Shown are the magnitude images (A) and signal phase-maps (B) acquired at four TE, as well as exemplary voxel-wise linear regression (C) and the reconstructed B_0-field (D).

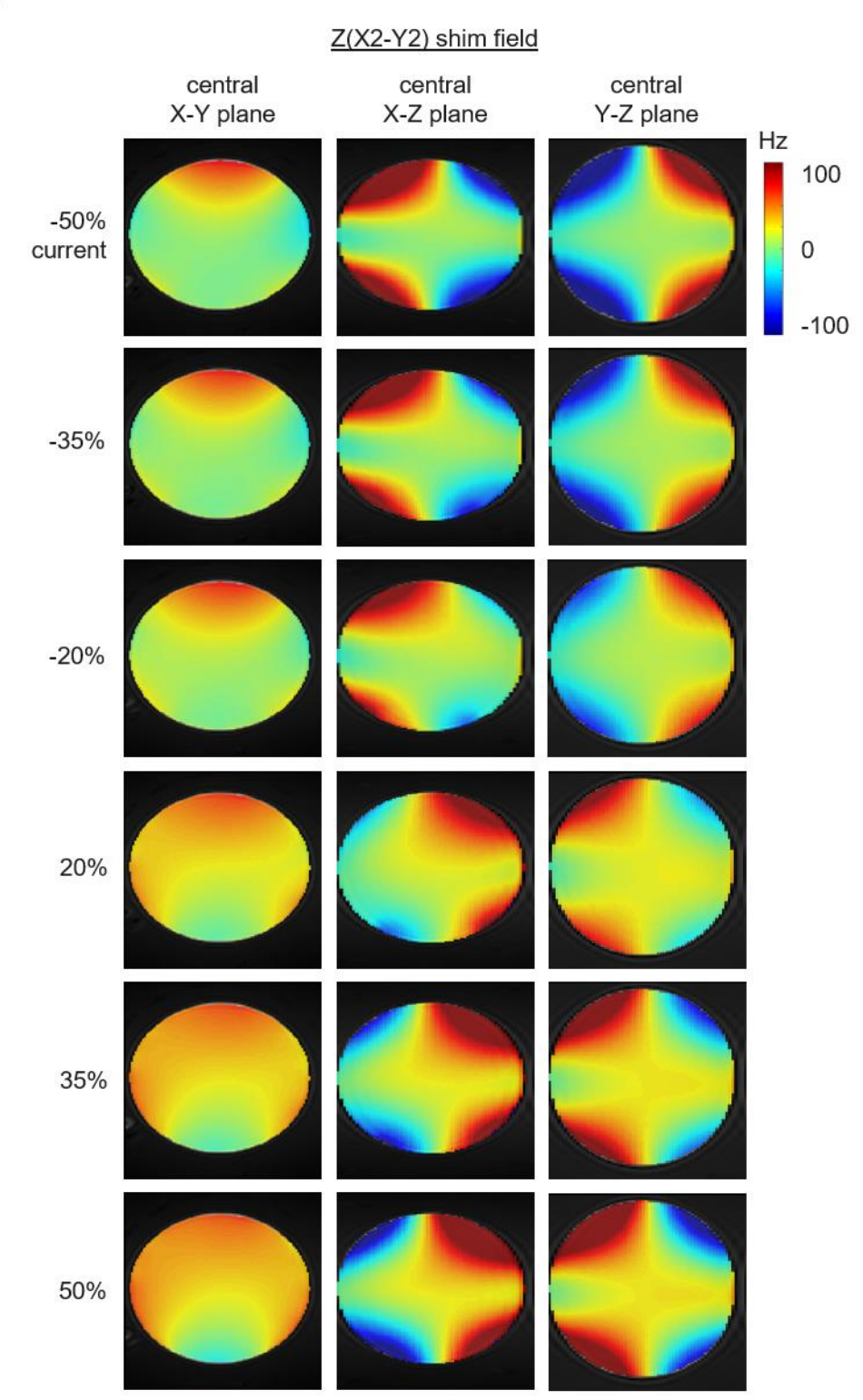

Figure 15. Calibration procedure for an individual spherical harmonics (SH) shim term. The current generating the 3rd-order SH term Z(X2-Y2) was varied in seven steps ranging from -50% to 50% of the shim coil's total dynamic range. Note that 0% is not shown.

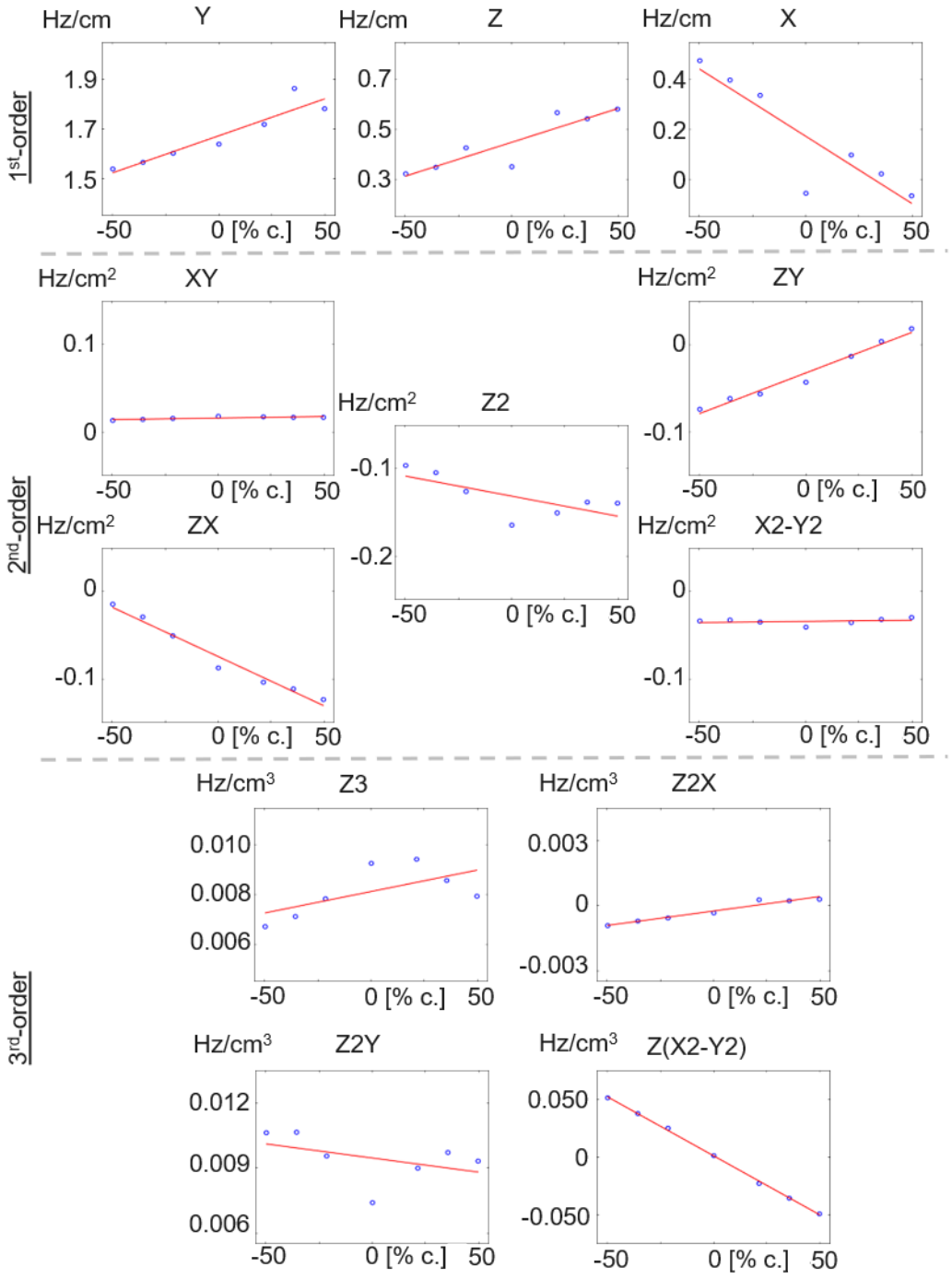

Figure 16. Generation of self- and cross-terms through the calibration procedure. Shown are the self- and all cross-terms generated by varying the 3rd-order spherical harmonic (SH) term Z(X2-Y2). The shim current was changed in seven steps ranging from -50% to 50% of the maximum current, and the resulting shim fields are given in Hz/cm^n (blue circles). Linear regression was performed to obtain the slope required for the calibration matrix (red lines). Note that present cross-terms were only derived for the scanner-integrated SH shim terms.

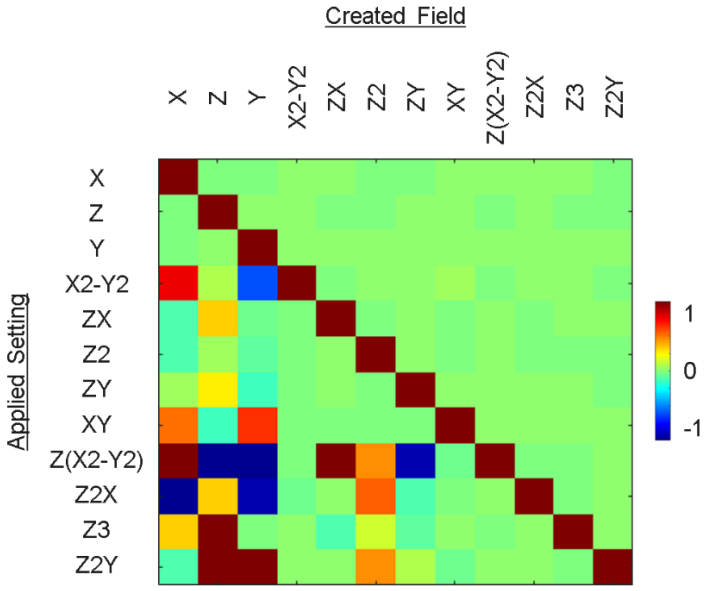

Figure 17. Calibration matrix for the partial 3rd-order SH shim system. The self-terms are displayed on the diagonal elements, and the cross-terms are located off-diagonal. In this case, the color encoding represents the normalized slopes.

4.2.3 Simulation of static shimming

The B_0 maps acquired after the slab-selective shimming unveiled the spatial field patterns inside the heart (Figure 18A and Figure 18B). Shim field simulations for the anatomy-matched SROIs, which were based on a calibration procedure as described in Section 2.4, led to predicted B_0 distributions (Figure 18D). For the latter decreased SDs and IQRs occurred versus the measured B_0 maps.

The shim field strengths for both the slab-selective shimming and the simulated shim (Figure 18C) were summarized in Figure 19. The medians of the X-, Y- and Z-gradient offsets differed just slightly (Figure 19, top row). Across all 3rd-order SH components, the zonal term Z3 featured the strongest difference. In four of the six subjects, the currents required for the simulated shim surpassed the hardware capabilities (Figure 19, bottom plot).

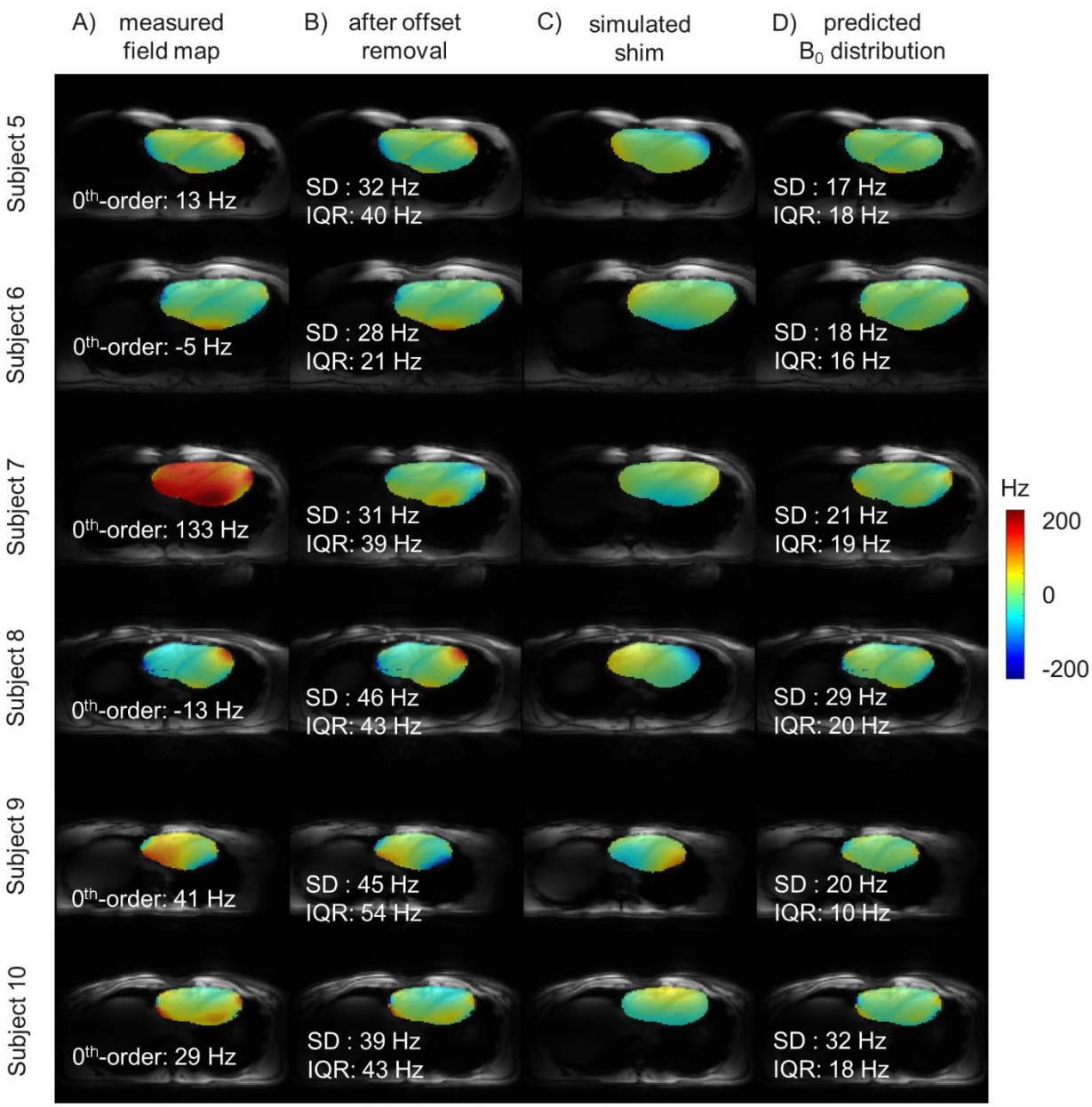

Figure 18. Calibration-based shim field simulations for an anatomy-matched SROI. The B_0 distributions acquired after the slab-selective shimming as shown in Figure 13A are provided for the central slices with present center frequency offset ("measured field map", A) and without ("after offset removal", B). Additive, the calibration-based computed shim fields ("simulated shim", C) and the anticipated B_0 distribution after their application ("predicted B_0 distribution", D) are shown. While A and B were obtained for a SROI cuboid, C and D were linked to the anatomy-matched SROI. Note that the scanner-integrated slab-selective shimming failed to correct the center frequency after modifying the higher-order shim field terms. This offset could be removed by adjusting the MR system's resonance frequency. Adapted from Reference (84).

When shimming with up to 2nd-order SH terms was compared to shimming with inclusion of 3rd-order terms, the latter was advantageous to homogenize the B_0 field in the anterolateral segment of the left-ventricular myocardium (Figure 20). However, hardware restrictions of the scanner-integrated shim system led to remainders of the 3rd-order terms. No 2nd-order term surpassed the hardware restrictions for any shim.

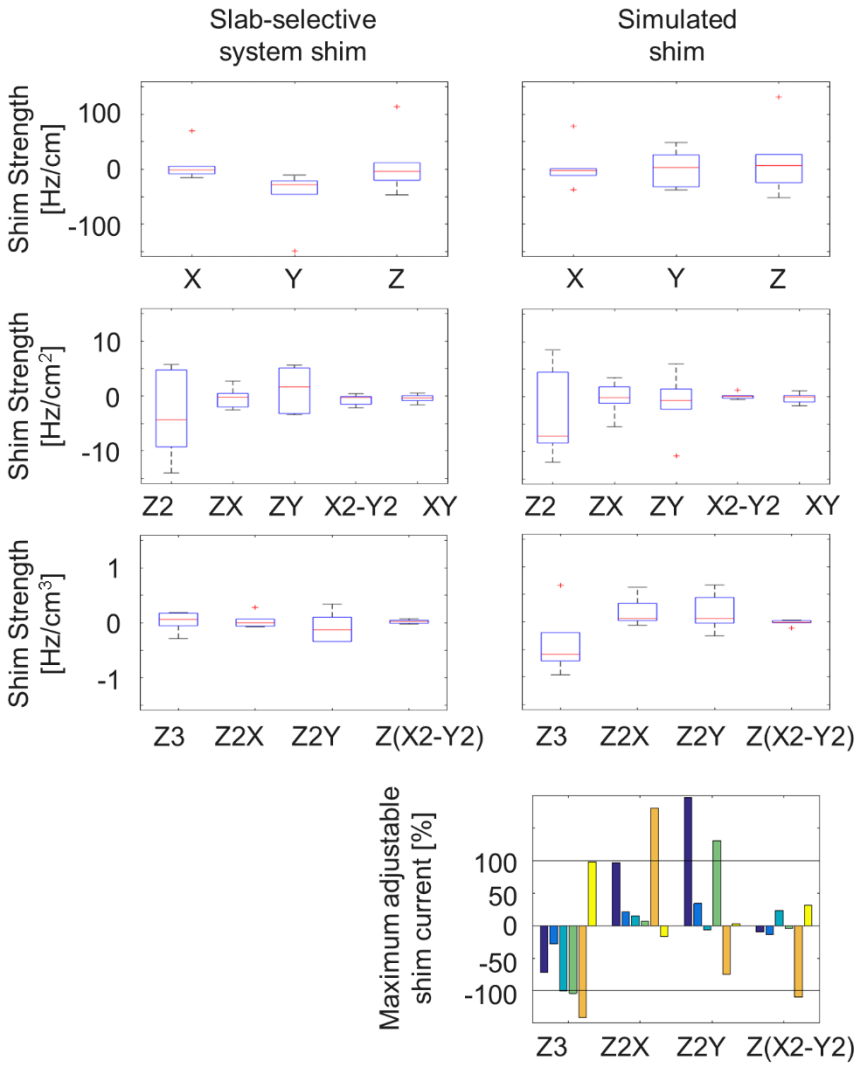

Figure 19. Required shim field strengths for SH components employed by the slab-selective and simulated anatomy-matched shimming shown in Figure 18. The relevant 3rd-order terms are visualized at length for the simulated shim in the bottom, where each color stands for one subject. The hardware restrictions of the scanner-integrated shim system are delineated with black lines. Adapted from Reference (84).

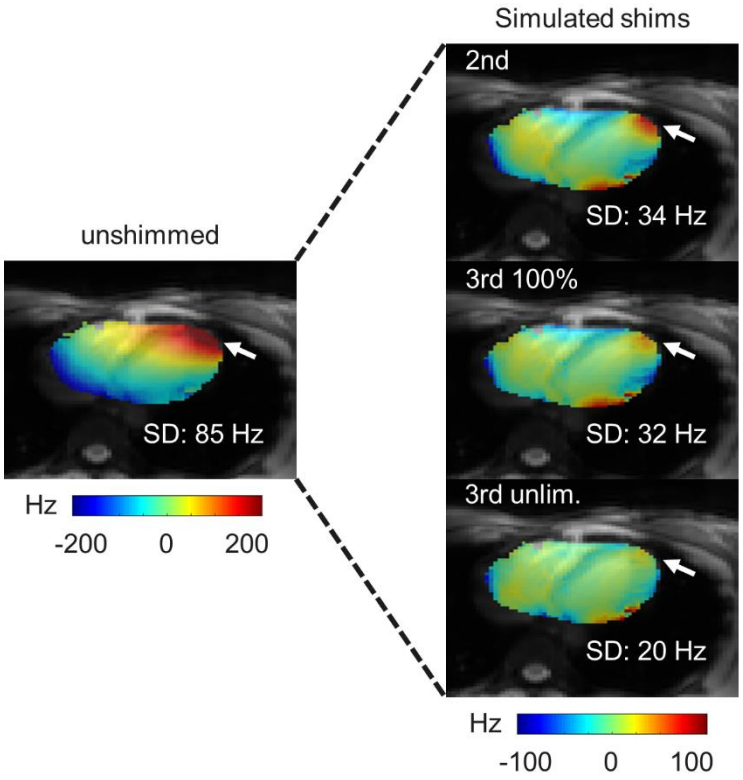

Figure 20. Relevance of higher-order SH terms for B_0 shimming of the heart. 3rd-order shimming was simulated with and without hardware restrictions. The un-shimmed B_0-field featured less than 5% of the maximum magnetic field strength feasible with each coil. Adapted from Reference (84).

4.2.4 Simulation of dynamic shimming

The temporal B_0-field fluctuations over the cardiac cycle, which occurred after volume-selective shimming, are summarized for the eight equally-spaced phases in Figure 21A. The application of two shimming approaches to the measured B_0-fields was simulated subsequently. The MR system employed in this study was not equipped with the hardware essential for CPSS, which consisted of the triggered B_0 map acquisition, anatomy-matched selection of the shim-region-of-interest (SROI), and calibration-based B_0 field modeling. Therefore, its simulation allowed to judge on whether the MR system should

be upgraded with the desired hardware, or an averaged static shim, which facilitated the mean of all eight CPSS fields, would be suitable for applications such as cine imaging instead. Averaged static shimming would lower these B_0-field inhomogeneities (Figure 21B). An even further reduction of myocardial B_0-field variations would be expected after simulated CPSS with anatomy-matched SROIs refreshed over the cardiac cycle (Figure 21C - cardiac phase 3, white arrow).

The optimal CPSS currents were found to alter in time over the cardiac cycle, which is highlighted for specific shim terms in Figure 21D (red arrows). Averaged over the six study group subjects, simulated CPSS resulted in a reduction of $\Delta SD = 1 \pm 1$ Hz of the B_0 distribution over the whole heart in contrast to averaged static shimming. In particular, CPSS was advantageous to lower myocardial B_0-field alterations, which is illustrated for subject 3 in Figure 21.

4.2.5 Advanced in vivo B_0 shimming

Preliminary findings of the advanced in vivo B_0 shimming are displayed in Figure 22. This heart-specific shim strategy included the triggered B_0 map acquisition, anatomy-matched selection of the shim-region-of-interest (SROI), and calibration-based B_0 field modeling. In the initial field maps, large B_0 variations were present in both the left- and right-ventricular myocardium prior to the shim (Figure 22B). These B_0-field variations were estimated to decrease substantially by means of the advanced shim simulations (Figure 22D). The simulated shim result was in good agreement with the experimental shim result (Figure 22E), and lowered the SD within the SROI from 45-52 Hz to 26-33 Hz slice-to-slice. Admittedly, shallow B_0-field distortions persisted within the myocardium, which were most notable in the left ventricle.

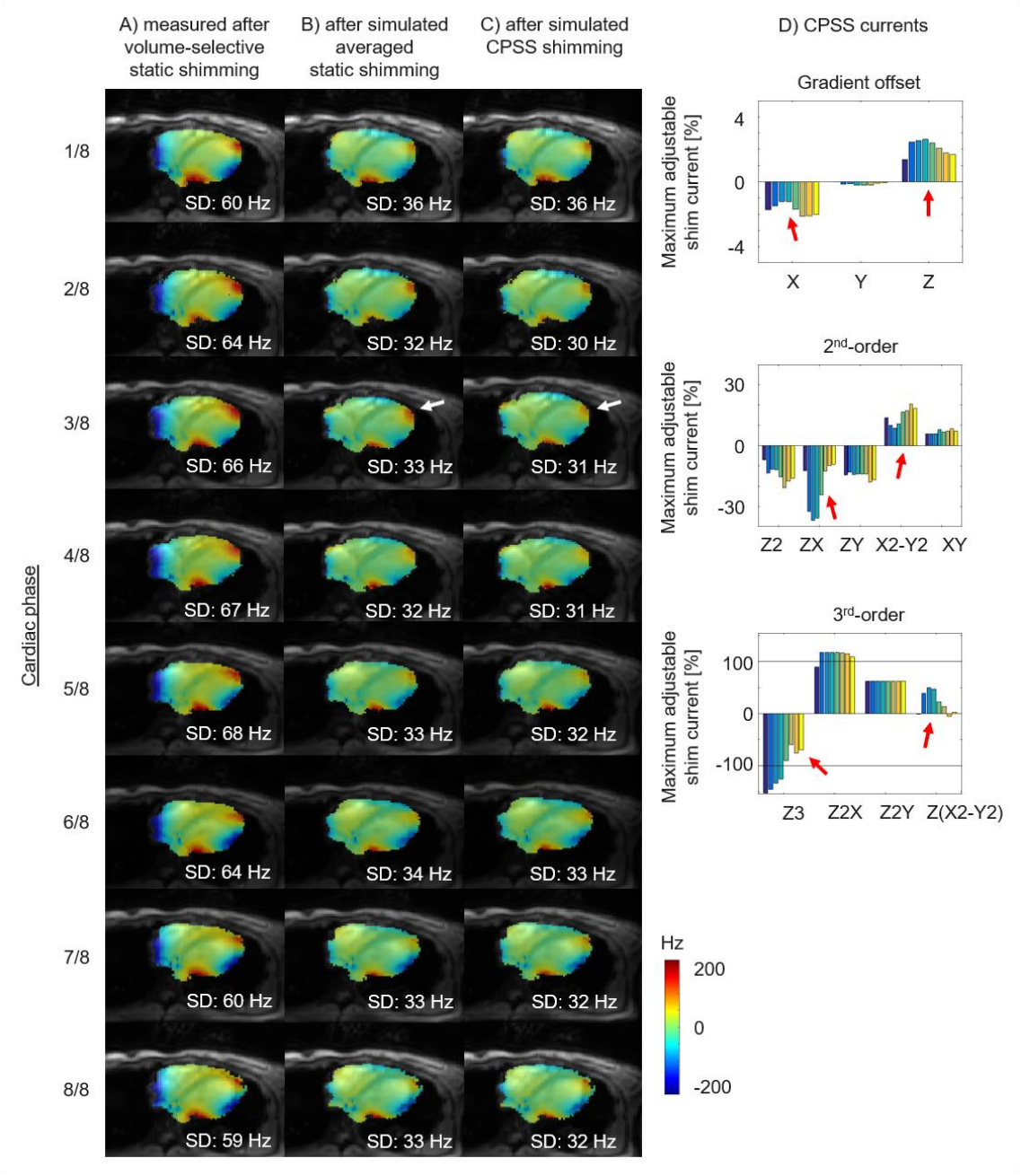

Figure 21. Cardiac phase-specific shimming (CPSS) in the heart for subject 3. Next to the B_0 field in the central slice observed after volume-selective shimming (A), the estimated outcome after both averaged static shimming (B) and CPSS (C) is demonstrated. The currents required to realize CPSS are given in (D), where each cardiac phase is illustrated by a different color. The averaged static shimming is characterized by using the mean shim field of all CPSS settings. Taking all six subjects of the study group into account, the standard deviation of the B_0 field distribution over the whole heart was reduced by $\Delta SD = 1 \pm 1$ Hz in contrast to averaged static shimming. Adapted from Reference (84).

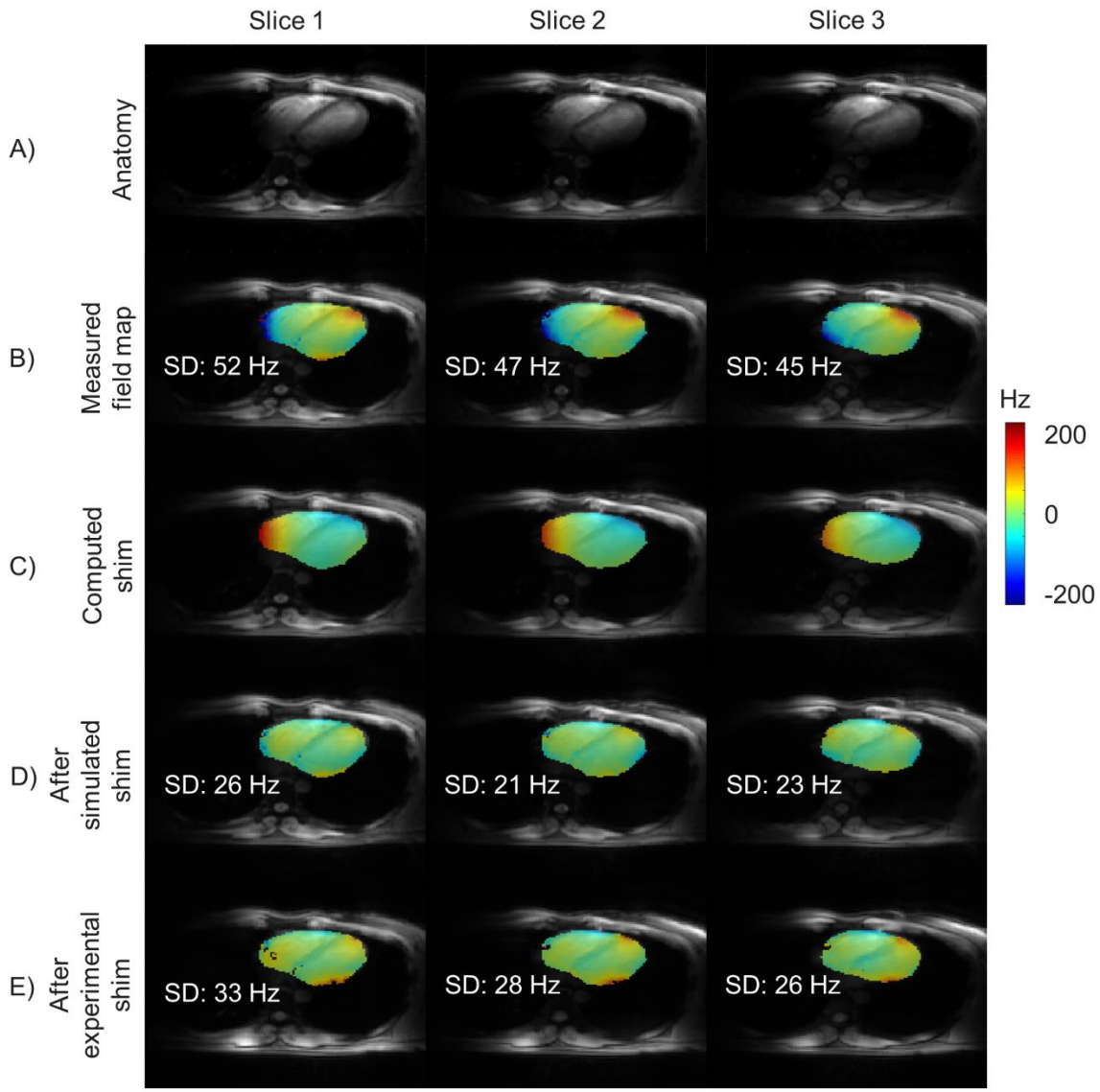

Figure 22. Initial in vivo results of 3rd-order B_0 shimming with the advanced shim strategy for subject 12. The magnitude images were used to extract the anatomy-matched SROI (A). Beside the primary measured B_0-field distributions (B) the correcting magnetic fields, which were computed via the advanced shim strategy (C), are visualized. The B_0-field distributions anticipated after the advanced shim (D) and measured after its experimental application (E) largely concurred. It has to be mentioned that the center frequency was subtracted from all field maps. Adapted from Reference (84).

5 Discussion

The accurate measurement and quantification of the myocardial B_0-field variations at 7 T in terms of both their spatial distribution and fluctuation over the cardiac cycle were analyzed in this work. High off-resonances appeared in localized spots, while temporal perturbations were observed between different cardiac phases. To reduce these B_0 inhomogeneities, three key factors were identified to be crucial and led to an advanced shim strategy: the triggered B_0-map acquisition, the anatomy-matched SROI selection, and calibration-based B_0-field modeling in dedicated shim software. Simulations of static shimming, which took these aspects into account, allowed to investigate the technical requirements for the employed shim system. The 3rd-order SH terms proved to be beneficial for B_0-field homogenization in comparison to the standard approach, which only uses the 2nd-order terms. The optimal shim currents, however, exceeded the capabilities of the built-in shim amplifiers in several cases. Simulations of dynamic shimming enabled insights into the potential advantages of CPSS. When the required shim field was calculated for different heart phases, monitoring of the individual required shim terms over the cardiac cycle unveiled oscillations. Initial in vivo results of the implemented advanced shim strategy widely matched the simulations.

5.1.1 Myocardial B_0-field inhomogeneities

In the presented work increased spatial B_0-field distortions were observed in the myocardium, which showed good agreement with previous studies (7,19). Their source was investigated with high-resolution simulations of the B_0-field conditions in the heart, which besides revealed that the positions of common B_0-field variations and dark band artifacts concur (85). Across the cardiac cycle, the B_0 distribution in the myocardium of both ventricles varied over time. This finding coincides with previous investigations, which explored the relationship between wall thickness and T_2^* of the left-ventricular myocardium (86-88). The temporal B_0 field fluctuations over the cardiac cycle substantiate the integration of a triggered pulse sequence into the shimming workflow. In this context, the diastolic SD of B_0 was not found to always being smaller than the systolic

SD across all subjects. A reason for this fact might be the transversal orientation of the B_0 field maps, which implicated highly subject-specific views. For SA or LA image orientations, either the SD at systolic or diastolic cardiac phases might always be lower, and this issue remains to be inspected when the shim strategy will be adjusted to anatomical views.

Data acquisition which lasts over several breath-holds could also lead to significant respiration-induced B_0 field variations. These variations could be analyzed by multiple repetitions of a scan over consecutive breath-holds. A previous examination demonstrated that local B_0 fluctuations accounted for 100 Hz and beyond, although their mean value varied only modestly between inhaled, half-exhaled, and exhaled breath-hold positions (11). To split the acquisition of multiple slices over repeated breath-holds, the B_0 maps may prospectively be measured together with diaphragm navigator images. The respiratory position would then be revealed during a calibration scan and a suitable correction could be employed. Monitoring of B_0 fluctuations with field probes and real-time B_0 field updating with a dynamic shim module could be an additional solution, which was proven to minimize respiration-induced B_0 field variations in the chest at 7 T (89).

5.1.2 Requirements for static shimming

Contrary to the volume-selective approach, the slab-selective shimming decreased these B_0 field variations in the heart considerably. The latter method made use of a SROI cuboid which had the same height as the three acquired slices, i.e., 18 mm, and was adjusted to accurately cover the whole heart in-plane. The slice-selective shimming, which employed a SROI capturing the central slice in height but an equal area in-plane, caused no additional decrease of the SD in 4 of the 6 subjects. Indeed, straight transversal slice orientations might promote partial volume effects (90). In addition, the slice-selective shim results were potentially affected by physiological alterations between the measurement of the first B_0 map applied for the shim current calculation and the second for the shim evaluation. If so, the 3D B_0 map should capture a SROI more than one slice thickness wider in both directions for a dependable shim. In-plane shim field simulations for an anatomy-matched SROI, which were expected to lower the B_0 field distortions

further in comparison with cuboid-based slab-selective shimming, are discussed further down the line.

Localized spots of minor B_0 field variations persisted in the myocardium despite advanced partial 3rd-order SH shimming for an anatomy-matched SROI. These residual alterations might be a consequence of the shim system's hardware restrictions, which would not always be capable of realizing the subject-specific shims as desired. Considering that the B_0-field inhomogeneities localized in small regions, the hardware capabilities of the scanner-integrated partial 3rd-order shim system might not impair cine imaging and consequent myocardial contour-tracking to estimate volumetric parameters and cardiac function. However, the characterization of tissue microstructure by quantitative MRI methods such as pixel-wise T_2^* mapping could profit more from improved hardware capabilities of the shim system. In this case, the relaxation time computation could become inaccurate when disease-affected tissue, e.g., a scar resulting from myocardial infarction, and areas of strong B_0 field-related off-resonances overlap. Another considerable factor could be the incidence of higher-order B_0 field constituents such as the 3rd-order SH terms X3, Y3, and XYZ, which the vendor-supplied set of shim coils did not incorporate. The extensive shimming capabilities required to tackle these B_0 field residuals might be realized by dedicated shim coil methodologies such as DYNAMITE (25,26), AC/DC (64), or iPRES (65). Various body shapes would complicate the arrangement of shim coils in the same localized setup for all experiments in comparison with brain applications, but could open exciting possibilities for future studies.

5.1.3 Potential of dynamic shimming

The advanced shimming methodology, which was developed within the scope of this work, was capable of performing a static shim designed for a certain cardiac phase or in an averaged fashion. To minimize B_0-field alterations over the cardiac cycle, CPSS was proven to enhance SSFP cine imaging at 3 T in a previous investigation (91). On the basis of these findings, the shim currents would ideally be adapted to each cardiac phase prospectively for cine imaging. Admittedly, the MR system at hand with its implemented

hardware did not enable dynamic shim updating, which would demand pre-emphasis and B_0 compensation with a dynamic shim interface together with specific shim amplifiers for a fast adjustment of shim currents (30). Brief updating times for the electronic components could then be ensured by storing the CPSS settings at the local hardware memory of the dynamic shim interface. In a similar way, slab-wise dynamic shim updating would be another concept to enhance B_0-field homogeneity beyond static shimming for a stack of multiple slices (8). Initially, dynamic shim updating was demonstrated slice-wise in the human brain (27,92).

In cases where the implemented hardware prevents the use of CPSS, the averaged static shimming would be an adequate approach. By tracking the temporal B_0-field alterations in conjunction with required CPSS currents, the mean of all CPSS shim fields could be derived. The impact of CPSS on SSFP cine imaging could be examined by subsequent repetitions of the experiment with dedicated trigger delays and shim settings for individual cardiac phases, thus avoiding the practical implementation of dynamic shim updating. Since the observed B_0 fluctuations were focused on smaller localized spots, the averaged static shimming might provide field homogeneity sufficient for deriving cardiac function and volumetric parameters from the myocardial contours determined via cine imaging. Quantitative MRI methods which evaluate the tissue microstructure on a pixel basis, in particular T_2^* mapping, could benefit the most from CPSS. Here, the localized spots of high B_0-field inhomogeneities and disease-affected tissue, e.g., a scar resulting from myocardial infarction, could coincide and have a severe impact on the relaxation time calculation. The advantage of CPSS for double-oblique image orientations remained to be proven, which is an important aspect for CMR applications and calls for an iteration of the analysis when this advanced shimming methodology would be aligned with the anatomical SA and LA views.

5.1.4 Adaptation to clinical imaging

The missing potential of the presented advanced shim strategy to homogenize the B_0 field for the double-oblique anatomical SA and LA image orientations was a drawback and impaired its adaptation to clinical CMR imaging. A possible solution for this issue would

be a modification of the geometric formalism of characterizing image rotations by two Euler angles, which has been proven to be suitable for shimming of single-oblique slices in the brain (93). In this context, the efficiency of the 3rd-order SH terms remained to be proven for varying image orientations in comparison with the transversal slice geometries. As a result, technical demands for the shim coils might vary. Alternatively, a stack of transversal slices could be positioned so as to contain the fraction of the heart region relevant for the anatomical views. A slice-wise anatomy-matched SROI selection in conjunction with a sufficient number of slices would allow shimming based on transversal field map data. Increased slice resolution and, therefore, measurement time would be required to minimize partial volume effects (90).

Slice-wise as well as cardiac phase-specific SROI segmentations were time-consuming when performed manually. To automate the segmentation process, deep learning (DL) approaches have been beneficial (94). Here, a sensitivity analysis would be a suitable approach to determine whether a DL-based segmentation model trained on a specific data set acquired at a certain field strength and with certain imaging parameters could provide accurate segmentation on another data set at which these parameters vary (95). Initial results produced by the employed software package in a dedicated case study were promising, however, the amount of training data in terms of B_0 field maps must be increased to achieve meaningful model predictions across large-scale subject cohorts.

Furthermore, whole-heart volume-selective shimming was also reported in detail for a large-scale study of 84 examinations, and two notable observations attracted attention (96). Firstly, the available 3rd-order SH shim coils were strongly employed across all subjects. Secondly, the Z3 shim term was used to capacity for numerous subjects. To avoid the permanent running of shim coils at capacity and the risk of hardware damaging, there would be potential to further improve passive shimming, i.e., ferromagnetic shim elements (97), for CMR imaging at 7 T. Beside the different inter-subject B_0-field conditions, inter-site variations could also be investigated for the heart similar as for the brain (98).

5.1.5 Implications for MR methods development

When it came to the accuracy of shim field computations, the resolution of the measured B_0 distribution played an important role. Here, SH terms like X2-Y2 or XY with an eminent dependency on the in-plane B_0 field were resolved in detail with the applied sequence parameters. In contrast, the SH terms like Z3 with a substantial influence on the B_0 field in z-direction were derived from through-slice data on the basis of the transversal 3D B_0 maps. More accurate magnetic field modeling might be achieved by increasing the number of slices, which was confined to three within a single breath-hold up-to-date.

Improved precision in B_0 field monitoring might also be reached by using a dynamic field camera, which would allow to correct B_0 field-related errors in pulse sequences (37). This concept would also be capable of tracking spatio-temporal B_0-field fluctuations in the human heart at 7 T and their relationship to physiological processes (99). To increase the spatial resolution of the B_0-field maps as the basis for shim computations, the field probe approach might be applied in conjunction with advanced cardiac shim strategies in the future. In addition, the dynamic field camera could be employed to track B_0-field variations during dynamic shimming on multiple slices. Here, periodical fluctuations were reported across the SH terms and demanded a pre-emphasis of the applied dynamic shim fields. The pre-emphasis would have to take all shim-to-shim interactions into account and could be accomplished via impulse response functions, which were shown to enable the appropriate correction of gradients and shims (39,40).

Recently, pre-emphasis of the gradient impulse response function was also integrated into cardiac real time imaging at 7 T (47). In contrast to the promising imaging quality of measurements conducted at 3 T (33), blurring due to an inhomogeneous B_0-field occurred within the myocardium. Since the vendor-supplied shimming workflow was applied for field homogenization, higher B_0-related off-resonances persisted in the images (84). Their correction would be feasible in two ways. On the one hand, the post-processing procedure for the acquired image data could take the underlying B_0-field into account. While a constant 0^{th}-order frequency offset across the FOV resulted in considerable blurring removal, additional improvement could be expected from techniques which consider the complex spatial B_0-field distribution across the human heart (100-104). On the other

hand, the advanced shim strategy presented in this work could assess the myocardial B_0-field fluctuations before the actual data acquisition (84). Both approaches would ideally be combined for effective blurring removal.

5.1.6 Overall discussion

The quantification of B_0-field inhomogeneities in the human heart and their correction, i.e., B_0 shimming, could be compared to several studies conducted at a magnetic field strength of 3 T. In the context of simultaneous B_0- and B_1^+-map acquisition for fast localized shim, frequency, and RF power determination in the heart at 3 T (77), dual TE B_0-mapping techniques were used to measure multi-slice field maps covering the B_0-field distribution across the entire heart in a single breath hold and eighteen cardiac cycles. Heart-specific 2^{nd}-order shimming, which also incorporated the 0^{th}-order B_0 offset correction, was conducted in seven healthy adult human subjects and improved the SD of the acquired B_0 field from 60 Hz to 35 Hz in comparison to an automated 1^{st}-order shimming routine.

Even at a magnetic field strength of 3 T, it was demonstrated that the use of SSFP-based pulse sequences for CMR is negatively affected by B_0-field imperfections inside the heart (91). To quantify temporal B_0-field variations across heart phases, B_0-field maps were acquired at multiple phases of the cardiac cycle. For 1^{st}- and 2^{nd}-order SH shimming, cardiac phase-specific shim settings were derived and evaluated both in simulation and in vivo. Within the entire heart, a mean variation of the SD of approximately 10 Hz was observed across twenty volunteers. Moreover, it was demonstrated that an anatomy-matched SROI is advantageous for accurate B_0-shimming of the heart, which could be seen from a reduction of field inhomogeneity by 32% when applying heart-specific 2^{nd}-order B_0-shimming in comparison to a standard SROI cuboid. Beyond, 2^{nd}-order CPSS lead to an additional improvement of 39%.

An approach combining active and passive shimming was evaluated by examining the effect of high-permittivity pads on specific absorption rate in RF- or B_1^+-shimmed dual-transmit cardiovascular magnetic resonance at 3T (105). Together, active B_1^+ shimming

in the form of dual transmit, and passive B_1^+ shimming, i.e., high permittivity pads, resulted in improved image quality in CMR at 3 T due to optimized B_1^+ homogeneity.

At the initial in vivo application of the advanced B_0 shimming strategy developed in this study, experimentally measured after-shim B_0-field agreed well with the simulated after-shim B_0-field. Concededly, marginal B_0-inhomogeneities remained within the myocardium, which were most remarkable in the left ventricle. It has to be noted that the period of time between the acquisition of the first B_0-map, which the shim computation was based on, and the second one, which measured the B_0-field after the experimental shim served, accounted for approximately one hour. While the same trigger delay was employed for both measurements, the volunteer's heart rate and, subsequently, the duration of the overall cardiac cycle could have changed over this period of time. Triggering the pulse sequence at a different time spot of the cardiac cycle would then result in a residual B_0-field due to the temporal B_0-field variations in the myocardium, which were explained previously. Therefore, it has to be ensured in the future that the trigger delay is adjusted for measuring the validation B_0-map to match the same time spot in the cardiac cycle as for measuring the initial B_0-field before shimming.

Further in vivo application of the advanced B_0 shimming strategy was prevented by spatial phase-wrapping in the measured B_0-field maps. The spatial phase-wrapping lead to leaps of the signal phase from positive to negative phase values and vice versa. As a result, physically not plausible leaps of the B_0-field occurred and could not be corrected for. Throughout this study, the spatial phase-unwrapping algorithm PRELUDE of the FSL (57,75) was employed. To improve the phase-unwrapping capabilities of the presented workflow, additional algorithms could be implemented and compared in the future. One option could be the rapid open-source minimum spanning tree algorithm (*ROMEO*) (58), which offers and improved phase-unwrapping paths and could as well perform single-step unwrapping across a fourth dimension to enable temporal phase unwrapping across the different TE for B_0 mapping.

6 Conclusion and Outlook

This work addressed the development of advanced shimming techniques for CMR to correct the spatio-temporal B_0 field variations present in the human heart at 7 T. State-of-the-art CPSS, which facilitated the triggered B_0 map acquisition, anatomy-matched SROI selection, and calibration-based SH field modeling, outperformed standard vendor-supplied shimming. These technical improvements are summarized hereafter.

The spatial pattern of the B_0-field within the human heart was found to be non-isotropic, while strong inhomogeneities occurred within the myocardium. Particularly these spots showed temporal fluctuations when monitored over multiple cardiac phases and gave rise to the embedding of a triggered B_0-mapping pulse sequence into the shimming procedure. A detailed decomposition of the spatial B_0-field distribution into SH constituents, in which shim-to-shim interactions were accounted for via a calibration process, revealed the benefit of higher-order correcting magnetic fields. To remove certain third-order components completely, either the passive shimming of the magnet could be tailored to CMR applications, or the amplifiers of the shim coils could be upgraded. The development of dedicated multi-coil shimming technology adapted to the human body could also address this challenge. While a precise SROI labeling was demonstrated to be essential for B_0-field homogenization, it remained a time-consuming work step and should in the future be addressed by transfer learning approaches using DL-based automated segmentation models to leverage advanced B_0 shimming. The first in vivo application of this shim strategy led to promising results for a healthy volunteer, for which the B_0 field measured after shimming was in good agreement with the simulated one. To unleash the full potential of this technique to clinical imaging, the possibility to compute shim fields for double-oblique slice orientations, i.e., the anatomical SA and LA views, would be a prerequisite. Furthermore, certain techniques for tissue characterization, e.g., temporally resolved T_2^* mapping, might profit by CPSS. Dynamic shimming on multiple cardiac phases, which ranged from systole to diastole, would result in reduced B_0-field inhomogeneities as proven by simulations. When the required hardware is not available, the varying shim fields, which oscillate over the cardiac cycle, could be assessed by a static shim which averages the cardiac phase-specific settings.

The presented technical developments showcase significant improvements on the way to quantitative cardiac magnetic resonance imaging of the human heart at ultra-high field strength. Together with other potential innovations, e.g., applications of the dynamic multi-coil technique, clinical studies about cardiac diseases seem in reach soon.

References

1. Mensah GA, Brown DW. An overview of cardiovascular disease burden in the United States. Health affairs 2007;26(1): 38-48.

2. Das KM. Cardiac MR: One-stop shop. Heart views 2004;5:17-23.

3. Poon M, Fuster V, Fayad, Z. Cardiac magnetic resonance imaging: a “one-stop-shop” evaluation of myocardial dysfunction. Current Opinion in Cardiology 2002;17(6):663-670.

4. Snyder CJ, DelaBarre L, Metzger GJ, van de Moortele PF, Akgun C, Ugurbil K, Vaughan JT. Initial results of cardiac imaging at 7 Tesla. Magnetic resonance in medi3ine 2009;61(3):517-524.

5. van Elderen SG, Versluis MJ, Webb AG, Westenberg JJ, Doornbos J, Smith NB, de Roos A, Stuber M. Initial results on in vivo human coronary MR angiography at 7 T. Magnetic resonance in medicine 2009;62(6):1379-1384.

6. Thalhammer C, Renz W, Winter L, Hezel F, Rieger J, Pfeiffer H, Graessl A, Seifert F, Hoffmann W, von Knobelsdorff-Brenkenhoff F, Tkachenko V, Schulz-Menger J, Kellman P, Niendorf T. Two-dimensional sixteen channel transmit/receive coil array for cardiac MRI at 7.0 T: design, evaluation, and application. Journal of magnetic resonance imaging : JMRI 2012;36(4):847-857.

7. Atalay MK, Poncelet BP, Kantor HL, Brady TJ, Weisskoff RM. Cardiac susceptibility artifacts arising from the heart-lung interface. Magnetic resonance in medicine 2001;45(2):341-345.

8. Mattar W, Juchem C, Terekhov M, Schreiber LM. Multi-coil B_0 shimming of the human heart: A theoretical assessment. In: Proceedings of the 24th Annual Meeting of ISMRM, Singapore, 2016. p 1151.

9. Juchem C, Herman P, Sanganahalli BG, Brown PB, McIntyre S, Nixon TW, Green D, Hyder F, de Graaf RA. DYNAmic Multi-coIl TEchnique (DYNAMITE) shimming of the rat brain at 11.7 T. NMR in biomedicine 2014;27(8):897-906.

10. Hezel F, Thalhammer C, Waiczies S, Schulz-Menger J, Niendorf T. High spatial resolution and temporally resolved T2* mapping of normal human myocardium at 7.0 Tesla: an ultrahigh field magnetic resonance feasibility study. PloS one 2012;7(12):e52324.

11. Schmitter S, Wu X, Ugurbil K, Van de Moortele PF. Design of parallel transmission radiofrequency pulses robust against respiration in cardiac MRI at 7 Tesla. Magnetic resonance in medicine 2015;74(5):1291-1305.

12. Schar M, Kozerke S, Fischer SE, Boesiger P. Cardiac SSFP imaging at 3 Tesla. Magnetic resonance in medicine 2004;51(4):799-806.

13. Carr HY. Steady-state free precession in nuclear magnetic resonance. Physical Review 1958;112(5):1693.

14. Bieri O, Scheffler, K. Fundamentals of balanced steady state free precession MRI. Journal of magnetic resonance imaging 2013;38(1): 2-11.

15. Bieri O, Markl M, Scheffler K. Analysis and compensation of eddy currents in balanced SSFP. Magnetic Resonance in Medicine 2005;54(1):129-137.

16. Nayak KS, Cunningham CH, Santos JM, Pauly JM. Real-time cardiac MRI at 3 tesla. Magnetic resonance in medicine 2004;51(4):655-660.

17. Ding S, Wolff SD, Epstein FH. Improved coverage in dynamic contrast-enhanced cardiac MRI using interleaved gradient-echo EPI. Magnetic resonance in medicine 1998;39(4):514-519.

18. Schmitter S, DelaBarre L, Wu X, Greiser A, Wang D, Auerbach EJ, Vaughan JT, Ugurbil K, Van de Moortele PF. Cardiac imaging at 7 Tesla: Single- and two-spoke radiofrequency pulse design with 16-channel parallel excitation. Magnetic resonance in medicine 2013;70(5):1210-1219.

19. Tao Y, Hess AT, Keith GA, Rodgers CT, Liu A, Francis JM, Neubauer S, Robson MD. Optimized saturation pulse train for human first-pass myocardial perfusion imaging at 7T. Magnetic resonance in medicine 2015;73(4):1450-1456.

20. Ferreira PF, Gatehouse PD, Mohiaddin RH, Firmin DN. Cardiovascular magnetic resonance artefacts. Journal of cardiovascular magnetic resonance : official journal of the Society for Cardiovascular Magnetic Resonance 2013;15:41.

21. Reeder SB, Faranesh AZ, Boxerman JL, McVeigh ER. In vivo measurement of T*2 and field inhomogeneity maps in the human heart at 1.5 T. Magnetic resonance in medicine 1998;39(6):988-998.

22. Noeske R, Seifert F, Rhein KH, Rinneberg H. Human cardiac imaging at 3 T using phased array coils. Magnetic resonance in medicine 2000;44(6):978-982.

23 Jaffer FA, Wen H, Balaban RS, Wolff SD. A method to improve the B0 homogeneity of the heart in vivo. Magnetic resonance in medicine 1996;36(3):375-383.

24. Schär M, Kozerke S, Boesiger P. Considerations on shimming for cardiac applications at 1.5 and 3.0 T. In: Proceedings of the 11th Annual Meeting of ISMRM, Toronto, Canada, 2003. p 174.

25. Juchem C, Nixon TW, McIntyre S, Boer VO, Rothman DL, de Graaf RA. Dynamic multi-coil shimming of the human brain at 7 T. Journal of magnetic resonance 2011;212(2):280-288.

26. Juchem C, Umesh Rudrapatna S, Nixon TW, de Graaf RA. Dynamic multi-coil technique (DYNAMITE) shimming for echo-planar imaging of the human brain at 7 Tesla. NeuroImage 2015;105:462-472.

27. Blamire AM, Rothman DL, Nixon T. Dynamic shim updating: a new approach towards optimized whole brain shimming. Magnetic resonance in medicine 1996;36(1):159-165.

28. de Graaf RA, Brown PB, McIntyre S, Rothman DL, Nixon TW. Dynamic shim updating (DSU) for multislice signal acquisition. Magnetic resonance in medicine 2003;49(3):409-416.

29. Koch KM, Sacolick LI, Nixon TW, McIntyre S, Rothman DL, de Graaf RA. Dynamically shimmed multivoxel 1H magnetic resonance spectroscopy and multislice magnetic resonance spectroscopic imaging of the human brain. Magnetic resonance in medicine 2007;57(3):587-591.

30. Juchem C, Nixon TW, Diduch P, Rothman DL, Starewicz P, de Graaf RA. Dynamic Shimming of the Human Brain at 7 Tesla. Concepts in magnetic resonance Part B, Magnetic resonance engineering 2010;37B(3):116-128.

31. Hennig J, Welz AM, Schultz G, Korvink J, Liu Z, Speck O, Zaitsev M. Parallel imaging in non-bijective, curvilinear magnetic field gradients: a concept study. MAGMA 2008;21(1-2):5-14.

32. Testud F, Gallichan D, Layton KJ, Barmet C, Welz AM, Dewdney A, Cocosco CA, Pruessmann KP, Hennig J, Zaitsev M. Single-shot imaging with higher-dimensional encoding using magnetic field monitoring and concomitant field correction. Magnetic resonance in medicine 2015;73(3):1340-1357.

33. Eirich P, Wech T, Heidenreich JF, Stich M, Petri N, Nordbeck P, Bley TA, Kostler H. Cardiac real-time MRI using a pre-emphasized spiral acquisition based on the gradient system transfer function. Magnetic resonance in medicine 2021;85(5):2747-2760.

34. Scholten H, Lohr D, Wech T, Köstler H. Fast measurement of the gradient system transfer function at 7 T. Magnetic resonance in medicine 2022;1-16.

35. Vannesjo SJ, Haeberlin M, Kasper L, Pavan M, Wilm BJ, Barmet C, Pruessmann KP. Gradient system characterization by impulse response measurements with a dynamic field camera. Magnetic resonance in medicine 2013;69(2):583-593.

36. Addy NO, Wu HH, Nishimura DG. Simple method for MR gradient system characterization and k-space trajectory estimation. Magnetic resonance in medicine 2012;68(1):120-129.

37. Dietrich BE, Brunner DO, Wilm BJ, Barmet C, Gross S, Kasper L, Haeberlin M, Schmid T, Vannesjo SJ, Pruessmann KP. A field camera for MR sequence monitoring and system analysis. Magnetic resonance in medicine 2016;75(4):1831-1840.

38. Morich MA, Lampman DA, Dannels WR, Goldie FD. Exact temporal eddy current compensation in magnetic resonance imaging systems. IEEE Trans Med Imaging 1988;7(3):247-254.

39. Vannesjo SJ, Dietrich BE, Pavan M, Brunner DO, Wilm BJ, Barmet C, Pruessmann KP. Field camera measurements of gradient and shim impulse responses using frequency sweeps. Magnetic resonance in medicine 2014;72(2):570-583.

40. Vannesjo SJ, Duerst Y, Vionnet L, Dietrich BE, Pavan M, Gross S, Barmet C, Pruessmann KP. Gradient and shim pre-emphasis by inversion of a linear time-invariant system model. Magnetic resonance in medicine 2017;78(4):1607-1622.

41. Engel M, Kasper L, Barmet C, Schmid T, Vionnet L, Wilm B, Pruessmann KP. Single-shot spiral imaging at 7 T. Magnetic resonance in medicine 2018;80(5):1836-1846.

42. Kasper L, Engel M, Barmet C, Haeberlin M, Wilm BJ, Dietrich BE, Schmid T, Gross S, Brunner DO, Stephan KE, Pruessmann KP. Rapid anatomical brain imaging using spiral acquisition and an expanded signal model. NeuroImage 2018;168:88-100.

43. Qian Y, Zhao T, Hue YK, Ibrahim TS, Boada FE. High-resolution spiral imaging on a whole-body 7T scanner with minimized image blurring. Magnetic resonance in medicine 2010;63(3):543-552.

44. Esmaeili M, Strasser B, Bogner W, Moser P, Wang Z, Andronesi OC. Whole-Slab 3D MR Spectroscopic Imaging of the Human Brain With Spiral-Out-In Sampling at 7T. Journal of magnetic resonance imaging : JMRI 2021;53(4):1237-1250.

45. Buonincontri G, Schulte RF, Cosottini M, Tosetti M. Spiral MR fingerprinting at 7T with simultaneous B1 estimation. Magn Reson Imaging 2017;41:1-6.

46. Ahunbay E, Pipe JG. Rapid method for deblurring spiral MR images. Magnetic resonance in medicine 2000;44(3):491-494.

47. Eirich P. Accelerated non-Cartesian cardiovascular MR Imaging at 3T and 7T: Universität Würzburg; 2022.

48. Bernstein MA, King KF, Zhou XJ. Handbook of MRI pulse sequences: Elsevier; 2004.

49. Brown RW, Cheng Y-CN, Haacke EM, Thompson MR, Venkatesan R. Magnetic resonance imaging: physical principles and sequence design: John Wiley & Sons; 2014.

50. De Graaf RA. In vivo NMR spectroscopy: principles and techniques: John Wiley & Sons; 2019.

51. Hoult D. The principle of reciprocity in signal strength calculations—a mathematical guide. Concepts in Magnetic Resonance: An Educational Journal 2000;12(4):173-187.

52. Gruetter R. Automatic, localized in vivo adjustment of all first- and second-order shim coils. Magnetic resonance in medicine 1993;29(6):804-811.

53. Reynaud O, Gallichan D, Schaller B, Gruetter R. Fast low-specific absorption rate B0 -mapping along projections at high field using two-dimensional radiofrequency pulses. Magnetic resonance in medicine 2015;73(3):901-908.

54. Gruetter R, Boesch C. Fast, Noniterative Shimming of Spatially Localized Signals - Invivo Analysis of the Magnetic-Field Along Axes. Journal of magnetic resonance 1992;96(2):323-334.

55. Juchem C. B0DETOX - B0 Detoxification Software for Magnetic Field Shimming. License CU17326: Columbia Tech Venture; 2017.

56. Abdul-Rahman HS, Gdeisat MA, Burton DR, Lalor MJ, Lilley F, Moore CJ. Fast and robust three-dimensional best path phase unwrapping algorithm. Applied optics 2007;46(26):6623-6635.

57. Jenkinson M. Fast, automated, N-dimensional phase-unwrapping algorithm. Magnetic resonance in medicine 2003;49(1):193-197.

58. Dymerska B, Eckstein K, Bachrata B, Siow B, Trattnig S, Shmueli K, Robinson SD. Phase unwrapping with a rapid opensource minimum spanning tree algorithm (ROMEO). Magnetic resonance in medicine 2021;85(4):2294-2308.

59. Golay MJE. Field Homogenizing Coils for Nuclear Spin Resonance Instrumentation. Rev Sci Instrum 1958;29(4):313-315.

60. Romeo F, Hoult DI. Magnet field profiling: analysis and correcting coil design. Magnetic resonance in medicine 1984;1(1):44-65.

61. Noguchi S. Formulation of the spherical harmonic coefficients of the entire magnetic field components generated by magnetic moment and current for shimming. Journal of Applied Physics 2014;115(16):163908.

62. Juchem C, Cudalbu C, de Graaf RA, Gruetter R, Henning A, Hetherington HP, Boer VO. B0 shimming for in vivo magnetic resonance spectroscopy: Experts' consensus recommendations. NMR in biomedicine 2020:e4350.

63. Pan JW, Lo KM, Hetherington HP. Role of very high order and degree B0 shimming for spectroscopic imaging of the human brain at 7 tesla. Magnetic resonance in medicine 2012;68(4):1007-1017.

64. Stockmann JP, Witzel T, Keil B, Polimeni JR, Mareyam A, LaPierre C, Setsompop K, Wald LL. A 32-channel combined RF and B0 shim array for 3T brain imaging. Magnetic resonance in medicine 2016;75(1):441-451.

65. Han H, Song AW, Truong TK. Integrated parallel reception, excitation, and shimming (iPRES). Magnetic resonance in medicine 2013;70(1):241-247.

66. Juchem C, de Graaf RA. B0 magnetic field homogeneity and shimming for in vivo magnetic resonance spectroscopy. Anal Biochem 2017;529:17-29.

67. Wikimedia Commons. Diagram of the human heart. Date published: June 21st 2019, Date accessed: August 31st 2021, URL: https://commons.wikimedia.org/wiki/File:Diagram_of_the_human_heart.svg.

68. Frauenrath T, Hezel F, Renz W, d'Orth Tde G, Dieringer M, von Knobelsdorff-Brenkenhoff F, Prothmann M, Schulz Menger J, Niendorf T. Acoustic cardiac triggering: a practical solution for synchronization and gating of cardiovascular magnetic resonance at 7 Tesla. Journal of cardiovascular magnetic resonance : official journal of the Society for Cardiovascular Magnetic Resonance 2010;12:67.

69. Siemens Healthineers. Magnetom Terra Brochure. Date published: 2019, Date accessed: November 15th, 2021, URL: https://cdn0.scrvt.com/39b415fb07de4d9656c7b516d8e2d907/463144ac5d3d3887/d2ffdb079bf4/siemens-healthineers-mri_magnetom_terra_brochure_2019_05.pdf.

70. Siemens Healthineers. FDA Clears MAGNETOM Terra 7T MRI Scanner Fom Siemens Healthineers. Date published: October 13th 2017, Date accessed: December 7th 2020, URL: https://www.siemens-healthineers.com/en-us/news/magnetomterrafdaclearance.html.

71. U.S. Food and Drug Administration (FDA). FDA clears first 7T magnetic resonance imaging device. Date published: October 12th 2017, Date accessed: December 7th 2020, URL: https://www.fda.gov/news-events/press-announcements/fda-clears-first-7t-magnetic-resonance-imaging-device.

72. Terekhov M, Elabyad IA, Schreiber LM. Global optimization of default phases for parallel transmit coils for ultra-high-field cardiac MRI. PloS one 2021;16(8):e0255341.

73. Terekhov M, Lohr D, Reiter T, Elabyad IA, Hock M, Schreiber LM. New commercial 8TX/16RX array for Clinical 7T Cardiac MRI: initial experience. In: Proceedings of the 29th Annual Meeting of ISMRM, Virtual, 2021. p 1584.

74. Lohr D, Terekhov M, Kosmala A, Stefanescu MR, Hock M, Schreiber LM. Cardiac MRI with the Siemens Terra 7 T system: Initial experiences and optimization of default protocols. In: Proceedings of the 26th Annual Meeting of ISMRM, Paris, France, 2018. p 3014.

75. Smith SM, Jenkinson M, Woolrich MW, Beckmann CF, Behrens TE, Johansen-Berg H, Bannister PR, De Luca M, Drobnjak I, Flitney DE, Niazy RK, Saunders J, Vickers J, Zhang Y, De Stefano N, Brady JM, Matthews PM. Advances in functional and structural MR image analysis and implementation as FSL. NeuroImage 2004;23 Suppl 1:S208-219.

76. Robinson SD, Bredies K, Khabipova D, Dymerska B, Marques JP, Schweser F. An illustrated comparison of processing methods for MR phase imaging and QSM: combining array coil signals and phase unwrapping. NMR in biomedicine 2017;30(4).

77. Schar M, Vonken EJ, Stuber M. Simultaneous B(0)- and B(1)+-map acquisition for fast localized shim, frequency, and RF power determination in the heart at 3 T. Magnetic resonance in medicine 2010;63(2):419-426.

78. Hock M, Terekhov M, Lohr D, Schröder A, Walles H, Schreiber LM. B_0-mapping and shimming efficiency for ex vivo MR imaging of the heart at ultra-high field - validation of standard shimming protocols of MAGNETOM™ Terra 7 T scanner. In: Proceedings of the DGMP and DGBMT Annual Meeting, Dresden, Germany, 2017. p 11.

79. Hock M, Terekhov M, Lohr D, Stefanescu MR, Schröder A, Walles H, Schreiber LM. Calibration of Siemens MAGNETOM™ Terra 7T shim system and analysis of static 3rd-order B_0-shimming of the heart using B0DETOX. In: Proceedings of the 26th Annual Meeting of ISMRM, Paris, France, 2018. p 1752.

80. Juchem C, Nixon TW, McIntyre S, Rothman DL, de Graaf RA. Magnetic field modeling with a set of individual localized coils. Journal of magnetic resonance 2010;204(2):281-289.

81. Nassirpour S, Chang P, Fillmer A, Henning A. A comparison of optimization algorithms for localized in vivo B0 shimming. Magnetic resonance in medicine 2018;79(2):1145-1156.

82. Hock M, Stefanescu MR, Terekhov M, Lohr D, Herz S, Juchem C, Schreiber LM. Third-order cardiac B_0-shimming at 7T in humans. In: Proceedings of the ISMRM Workshop on Ultrahigh Field Magnetic Resonance: Technological Advances, Translational Research Promises & Clinical Applications, Dubrovnik, Croatia, 2019. p 3.

83. Hock M, Terekhov M, Reiter T, Lohr D, Juchem C, Schreiber LM. Correction of myocardial B_0-inhomogeneities at 7T with ECG-gated spherical harmonics shimming. In: Proceedings of the 2019 Minnesota Workshop on High and Ultra-high Field Imaging, Center for Magnetic Resonance Research, Minneapolis, MN, USA, 2019. Talk.

84. Hock M, Terekhov M, Stefanescu MR, Lohr D, Herz S, Reiter T, Ankenbrand M, Kosmala A, Gassenmaier T, Juchem C. B0 shimming of the human heart at 7T. Magnetic resonance in medicine 2021;85(1):182-196.

85. Shang Y, Theilenberg S, Mattar W, Terekhov M, Jambawalikar SR, Schreiber LM, Juchem C. High resolution simulation of B0 field conditions in the human heart based on segmented CT images. In: Proceedings of the 27th Annual Meeting of ISMRM, Montreal, Canada, 2019. p 2184.

86. Serradas Duarte T, Huelnhagen T, Niendorf T. Assessment of myocardial B0 over the cardiac cycle at 7.0 Tesla: Implications for susceptibility-based cardiac MR techniques. In: Proceedings of the 24th Annual Meeting of ISMRM, Singapore, 2016. p 2541.

87. Huelnhagen T, Hezel F, Serradas Duarte T, Pohlmann A, Oezerdem C, Flemming B, Seeliger E, Prothmann M, Schulz-Menger J, Niendorf T. Myocardial effective transverse relaxation time T2* Correlates with left ventricular wall thickness: A 7.0 T MRI study. Magnetic resonance in medicine 2017;77(6):2381-2389.

88. Huelnhagen T, Paul K, Ku MC, Duarte TS, Niendorf T. Myocardial T-2* Mapping with Ultrahigh Field Magnetic Resonance: Physics and Frontier Applications. Front Phys 2017;5.

89. Boer VO, van de Bank BL, van Vliet G, Luijten PR, Klomp DW. Direct B0 field monitoring and real-time B0 field updating in the human breast at 7 Tesla. Magnetic resonance in medicine 2012;67(2):586-591.

90. Attili AK, Schuster A, Nagel E, Reiber JH, van der Geest RJ. Quantification in cardiac MRI: advances in image acquisition and processing. The international journal of cardiovascular imaging 2010;26 Suppl 1:27-40.

91. Kubach MR, Bornstedt A, Hombach V, Merkle N, Schar M, Spiess J, Nienhaus GU, Rasche V. Cardiac phase-specific shimming (CPSS) for SSFP MR cine imaging at 3 T. Physics in medicine and biology 2009;54(20):N467-478.

92. Morrell G, Spielman D. Dynamic shimming for multi-slice magnetic resonance imaging. Magnetic resonance in medicine 1997;38(3):477-483.

93. Koch KM, McIntyre S, Nixon TW, Rothman DL, de Graaf RA. Dynamic shim updating on the human brain. Journal of magnetic resonance 2006;180(2):286-296.

94. Chen C, Qin C, Qiu H, Tarroni G, Duan J, Bai W, Rueckert D. Deep Learning for Cardiac Image Segmentation: A Review. Front Cardiovasc Med 2020;7:25.

95. Ankenbrand MJ, Shainberg L, Hock M, Lohr D, Schreiber LM. Sensitivity analysis for interpretation of machine learning based segmentation models in cardiac MRI. BMC Medical Imaging 2021;21(1):27.

96. Reiter T, Lohr D, Hock M, Ankenbrand MJ, Stefanescu MR, Kosmala A, Kaspar M, Juchem C, Terekhov M, Schreiber LM. On the way to routine cardiac MRI at 7 Tesla - a pilot study on consecutive 84 examinations. PloS one 2021;16(7):e0252797.

97. Juchem C, Muller-Bierl B, Schick F, Logothetis NK, Pfeuffer J. Combined passive and active shimming for in vivo MR spectroscopy at high magnetic fields. Journal of magnetic resonance 2006;183(2):278-289.

98. Voelker MN, Kraff O, Goerke S, Laun FB, Hanspach J, Pine KJ, Ehses P, Zaiss M, Liebert A, Straub S, Eckstein K, Robinson S, Nagel AN, Stefanescu MR, Wollrab A, Klix S, Felder J, Hock M, Bosch D, Weiskopf N, Speck O, Ladd ME, Quick HH. The traveling heads 2.0: Multicenter reproducibility of quantitative imaging methods at 7 Tesla. NeuroImage 2021;232:117910.

99. Gross S, Dietrich BE, Barmet C, Pruessmann KP. Spatially resolved observation of cardiovascular magneto-dynamics with NMR field probes. In: Proceedings of the 21st Annual Meeting of ISMRM, Salt Lake City, UT, USA, 2013. p 1410.

100. Man LC, Pauly JM, Macovski A. Multifrequency interpolation for fast off-resonance correction. Magnetic resonance in medicine 1997;37(5):785-792.

101. Man LC, Pauly JM, Macovski A. Improved automatic off-resonance correction without a field map in spiral imaging. Magnetic resonance in medicine 1997;37(6):906-913.

102. Nayak KS, Tsai CM, Meyer CH, Nishimura DG. Efficient off-resonance correction for spiral imaging. Magnetic resonance in medicine 2001;45(3):521-524.

103. Moriguchi H, Dale BM, Lewin JS, Duerk JL. Block regional off-resonance correction (BRORC): a fast and effective deblurring method for spiral imaging. Magnetic resonance in medicine 2003;50(3):643-648.

104. Chen W, Meyer CH. Fast automatic linear off-resonance correction method for spiral imaging. Magnetic resonance in medicine 2006;56(2):457-462.

105. Brink WM, van den Brink S, Webb AG. The effect of high-permittivity pads on specific absorption rate in radiofrequency-shimmed dual-transmit cardiovascular magnetic resonance at 3T. Journal of cardiovascular magnetic resonance 2015;17(1): 1-8.

List of Figures

List of Tables

Acknowledgements

Over the past five years a number of people guided and supported me with their advice, for which I am exceptionally grateful. It was a pleasure to work with these extraordinary supervisors, colleagues, and friends. In particular, I would like to say thank you to …

Prof. Laura Schreiber for the unique chance to pursue my PhD on this exciting topic, the trust in my skills, fruitful discussions about my research, and the constant support over the years. Looking back, I am so thankful for everything I have learned from you.

Prof. Herbert Köstler and Prof. Wolfgang Bauer for being part of my thesis committee and accompanying me on my way. You constantly showed great interest in my work, and I appreciate your many helpful suggestions during our regular meetings.

The Graduate School of Life Science for providing an outstanding infrastructure, and their staff for being so supportive with any kind of problems occurring over the years.

Prof. Christoph Juchem for coaching me from New York City and turning me into a shimming junkie. I have our meetings in Würzburg, Dubrovnik, and Minnesota in good memory. There is so much to learn from you, which goes far beyond B_0 shimming.

Dr. Maxim Terekhov, Dr. Ibrahim Elabyad, Dr. David Lohr, Dr. Markus Ankenbrand, Dr. Theresa Reiter for being outstanding colleagues and friends. Working together with you is a highlight – and you took care of having fun even during busy and stressful times at work.

All present and past members of the Chair of Cellular and Molecular Imaging for the remarkable team spirit. A special thank you goes to Dr. Alessandra Bierwagen, Verena Burkard, and Mihaela Pali for taking away many organizational burdens.

Bettina Dammenhain and Anne Dorsch for assistance with bureaucratic obstacles. You made sure that travel costs were reimbursed soon and no holidays got lost. Omar Boukili, thank you for tackling many technical difficulties with a good mood.

My parents Thea and Burkhard for your never-ending interest in my work, unlimited support throughout my studies, and for being there for me in good and bad times ♥

Publications

Journal Papers

Hock M, Terekhov M, Stefanescu MR, Lohr D, Herz S, Reiter T, Ankenbrand MJ, Kosmala A, Gassenmaier T, Juchem C, Schreiber LM.
B_0 shimming of the human heart at 7T.
Magn Reson in Med 2021; 85:182-196, DOI: 10.1002/mrm.28423.

Ankenbrand MJ, Shainberg L, **Hock M**, Lohr D, Schreiber LM.
Sensitivity Analysis for Interpretation of Machine Learning Based Segmentation Models in Cardiac MRI.
BMC Med Imaging 2021;21(1):27, DOI: 10.1186/s12880-021-00551-1.

Voelker MN, Kraff O, Goerke S, Laun FB, Hanspach J, Pine KJ, Ehses P, Zaiss M, Liebert A, Straub S, Eckstein K, Robinson SD, Nagel AM, Stefanescu MR, Wollrab A, Klix S, Felder J, **Hock M**, Bosch D, Weiskopf N, Speck O, Ladd ME, Quick HH.
The Traveling Heads 2.0: Multicenter Reproducibility of Quantitative Imaging Methods at 7 Tesla.
NeuroImage 2021;232:117910, DOI: 10.1016/j.neuroimage.2021.117910.

Reiter T, Lohr D, **Hock M**, Ankenbrand MJ, Stefanescu MR, Kosmala A, Kaspar M, Juchem C, Terekhov M, Schreiber LM.
On the way to routine cardiac MRI at 7 Tesla – a pilot study on consecutive 84 examinations.
PLoS One 2021;16(7):e0252797, DOI: 10.1371/journal.pone.0252797.

Elabyad IA, Terekhov M, Lohr D, Bille M, **Hock M**, Schreiber LM.
A Novel Antisymmetric 16-Element Transceiver Dipole Antenna Array for Parallel Transmit Cardiac MRI in Pigs at 7T.
NMR Biomed 2022;e4726, DOI: 10.1002/nbm.4726.

Conference Proceedings

Conference contributions as first-author:

Hock M, Terekhov M, Ankenbrand M, Lohr D, Reiter T, Juchem C, Schreiber LM. Considerations for cardiac phase-specific B_0-shimming at 7 T.
ISMRM 28th Annual Meeting & Exhibition, Virtual Conference & Exhibition, Abstract #1277 (Talk)

Hock M, Terekhov M, Reiter T, Lohr D, Juchem C, Schreiber LM.
Correction of Myocardial B_0-Inhomogeneities at 7 T with ECG-Gated Spherical Harmonics Shimming.
2019 Minnesota Workshop on High and Ultra-high Field Imaging, Minneapolis, MN, USA (Talk)

Hock M, Terekhov M, Stefanescu M, Lohr D, Herz S, Juchem C, Schreiber LM.
Reduzierung von lokalen B_0-Inhomogenitäten in der kardialen MRT bei 7 T durch Shimming der dritten Ordnung.
50. Jahrestagung der Deutschen Gesellschaft für Medizinische Physik, Stuttgart, Deutschland (Traditional Poster)

Hock M, Stefanescu M, Terekhov M, Lohr D, Herz S, Juchem C, Schreiber LM.
Strategy for Third-Order Shimming of the B_0-field within the human heart at 7 T.
DZHI / DZHK Joint Symposium "Heart Failure Interfaces", Würzburg, Deutschland (Traditional Poster)

Hock M, Stefanescu M, Terekhov M, Lohr D, Herz S, Juchem C, Schreiber LM.
Third-order Cardiac B_0-Shimming at 7 T in Humans.
ISMRM Workshop on Ultrahigh Field Magnetic Resonance: Technological Advances, Translational Research Promises & Clinical Applications, Dubrovnik, Croatia, Abstract #3 (Power Pitch & Traditional Poster Presentation)

Hock M, Terekhov M, Lohr D, Stefanescu M, Schroeder A, Walles H, Juchem C, Schreiber LM. Calibration of Siemens MAGNETOM™ Terra 7T Shim System and Analysis of Static 3rd-order B_0-Shimming of the Heart Using B0DETOX.
ISMRM 26th Annual Meeting & Exhibition, Paris, France, Abstract #1752 (Traditional Poster)

Hock M, Terekhov M, Lohr D, Schroeder A, Walles H, Schreiber LM.
B_0-Mapping and Shimming Efficiency for ex Vivo MR Imaging of the Heart at Ultra-High Field: Validation of Standard Shimming Protocols of MAGNETOM™ Terra 7T Scanner.
Jahrestagung der Biomedizinischen Technik und Dreiländertagung der Medizinischen Physik, Dresden, Germany (Traditional Poster)

Other conference contributions as co-author:

Terekhov M, Lohr D, Reiter T, Elabyad IA, **Hock M**, Schreiber LM.
New Commercial 8Tx/16RX Array for Clinical Application in 7T Cardiac MRI: Initial Experience in Healthy Volunteers.
2021 Minnesota Workshop on High and Ultra-high Field Imaging, Virtual Conference (Electronic Poster)

Lohr D, Bille M, Terekhov M, **Hock M**, Elabyad IA, Baltes S, Kollmann A, Reiter T, Schnitter F, Bauer WR, Hofmann U, Schreiber LM.
UHF Cardiac MRI in a Preclinical Large Animal Model of Acute and Chronic Myocardial Infarction.
2021 Minnesota Workshop on High and Ultra-high Field Imaging, Virtual Conference (Electronic Poster)

Aures J, Terekhov M, Lohr D, Bille M, **Hock M**, Elabyad IA, Bauer WR, Hofmann U, Schreiber LM.
Analysis of Post-Infarction Cardiac Tissue Remodeling at 7T using T_2^* Contrast: Longitudinal Pilot Study in a Porcine Myocardial Infarction Model.
2021 Minnesota Workshop on High and Ultra-high Field Imaging, Virtual Conference (Electronic Poster)

Terekhov M, Lohr D, **Hock M**, Bille M, Baltes S, Elabyad IA, Schnitter S, Aures J, Reiter T, Bauer WR, Hofmann U, Schreiber LM.
Visualization of Post-Infarction Cardiac Tissue Remodeling at 7T using T_2^* contrast: Longitudinal Study in a Pig Myocardial Infarction Model.
ISMRM 29th Annual Meeting & Exhibition, Virtual Conference & Exhibition, Abstract #0021 (Digital Poster)

Lohr D, Bille B, Terekhov M, **Hock M**, Elabyad IA, Baltes S, Kollmann A, Reiter T, Schnitter F, Bauer WR, Hofmann U, Schreiber LM.
Ultrahigh Field Cardiac MRI in a Large Animal Model of Acute and Chronic Infarction.
ISMRM 29th Annual Meeting & Exhibition, Virtual Conference & Exhibition, Abstract #0960 (Digital Poster)

Terekhov M, Reiter T, **Hock M**, Lohr D, Bauer WR, Schreiber LM.
Towards Clinical Application of the T_2^* quantification in the 7T Cardiac MRI: Reproducibility Study in Healthy Volunteers.
ISMRM 29th Annual Meeting & Exhibition, Virtual Conference & Exhibition, Abstract #0984 (Digital Poster)

Elabyad IA, Terekhov M, **Hock M**, Lohr D, Schreiber LM.
Development of a Dedicated Mono-surface 16-Element Transceiver Dipole Antenna Array for Parallel Transmission Cardiac MRI in Pigs at 7 Tesla.
ISMRM 29th Annual Meeting & Exhibition, Virtual Conference & Exhibition, Abstract #1577 (Digital Poster)

Terekhov M, Lohr D, Reiter T, Elabyad IA, **Hock M**, Schreiber LM.
New commercial 8Tx/16Rx array for Clinical 7T Cardiac MRI: initial experience.
ISMRM 29th Annual Meeting & Exhibition, Virtual Conference & Exhibition,
Abstract #1584 (Digital Poster)

Ankenbrand MJ, Shainberg L, **Hock M**, Lohr D, Schreiber LM.
Sensitivity of a Deep Learning Model for Multi-Sequence Cardiac Pathology Segmentation to Input Data Transformations.
ISMRM 29th Annual Meeting & Exhibition, Virtual Conference & Exhibition,
Abstract #2652 (Digital Poster)

Reiter T, Lohr D, **Hock M**, Ankenbrand MJ, Stefanescu MR, Terekhov M, Schreiber LM.
On the way to routine cardiac MRI at 7Tesla- using what we have.
ISMRM 28th Annual Meeting & Exhibition, Virtual Conference & Exhibition,
Abstract #4295 (Digital Poster)

Stefanescu MR, Terekhov M, Elabyad IA, Lohr D, **Hock M**, Schreiber LM.
Acceleration Factor Analysis of Different Dedicated 8Tx/16Rx Coil Arrays for Cardiac MRI at 7T.
ISMRM 27th Annual Meeting & Exhibition, Virtual Conference & Exhibition,
Abstract #2151 (Digital Poster)

Lohr D, Terekhov M, Kosmala A, Stefanescu MR, **Hock M**, Schreiber LM.
Cardiac MRI with the Siemens Terra 7T System: Initial Experience and Optimization of Default Protocols.
ISMRM 26th Annual Meeting & Exhibition, Virtual Conference & Exhibition,
Abstract #3014 (Traditional Poster)

Affidavit

Affidavit

I hereby confirm that my thesis entitled *Methods for Homogenization of Spatio-Temporal B_0 Magnetic Field Variations in Cardiac MRI at Ultra-High Field Strength* is the result of my own work. I did not receive any help or support from commercial consultants. All sources and / or materials applied are listed and specified in the thesis.

Furthermore, I confirm that this thesis has not yet been submitted as part of another examination process neither in identical nor similar form.

Würzburg, March 17th 2023 Michael Hock, M.Sc.

Eidesstattliche Erklärung

Hiermit erkläre ich an Eides statt, die Dissertation *Methoden zur Homogenisierung räumlicher und zeitlicher Variationen des B_0-Feldes in der kardialen Ultrahochfeld-MRT* eigenständig, d.h. insbesondere selbständig und ohne Hilfe eines kommerziellen Promotionsberaters, angefertigt und keine anderen als die von mir angegebenen Quellen und Hilfsmittel verwendet zu haben.

Ich erkläre außerdem, dass die Dissertation weder in gleicher noch in anderer Form bereits in einem anderen Prüfungsverfahren vorgelegen hat.

Würzburg, March 17th 2023 Michael Hock, M.Sc.

Curriculum Vitae